Electronic
Research Archive

https://www.aimspress.com/journal/era

ERA, 34(6): 4248–4289.
DOI: 10.3934/era.2026190
Received: 04 March 2026
Revised: 19 April 2026
Accepted: 06 May 2026
Published: 19 May 2026

Research article

The breakdown of linear quasi-cycles: Demographic noise and absorbing boundaries in finite predator–prey systems

Louis Shuo Wang[1,†], **Jiguang Yu**[2,∗,†], **Ye Liang**[3,†] **and Jilin Zhang**[4]

[1] Department of Mathematics, University of Tennessee, Knoxville, TN 37996, USA

[2] College of Engineering, Boston University, Boston, MA 02215, USA

[3] Department of Industrial and Systems Engineering, The University of Iowa, Iowa City, IA 52242, USA

[4] Department of Mathematics, Imperial College London, London SW7 2AZ, UK

† These authors contributed equally to this work.

* **Correspondence:** Email: jyu678@bu.edu.

Abstract: Environmental enrichment can destabilize predator–prey coexistence through a Hopf bifurcation, yet real ecosystems are finite and intrinsically stochastic. We investigate how mechanistically derived demographic noise shapes near-Hopf dynamics in the Rosenzweig–MacArthur model by systematically comparing two diffusion closures that share identical deterministic drift but differ solely in their predation-induced covariance structure. Starting from a continuous-time Markov chain description, we derive a full-covariance stochastic differential equation whose diffusion tensor inherits stoichiometric coupling, generating a negative prey–predator cross-covariance. Our exact nonlinear simulations demonstrate that the dominant near-Hopf phenomenon is the profound breakdown of the linear noise approximation itself. While the linear noise approximation predicts unbounded variance and spectral amplification, the true nonlinear quasi-cycles remain strictly bounded, rapidly driving the system into absorbing extinction boundaries. We conclude that accurate early warning inference in finite ecosystems depends not on resolving fine-scale stoichiometric covariance, but on properly accounting for nonlinear saturation and noise-induced boundary hitting.

Keywords: complex systems; stochastic dynamical systems; Hopf bifurcation; diffusion approximation; covariance structure; linear noise approximation; power spectral density; multiscale modeling

1. Introduction

Understanding the mechanisms by which ecosystems transition from stable coexistence to sustained oscillatory behavior is a central problem in theoretical ecology. In deterministic predator–prey models of the Rosenzweig–MacArthur (R–M) type [1–3], progressive environmental enrichment constitutes an increase in the prey carrying capacity. This increase drives the coexistence equilibrium through a supercritical Hopf bifurcation and generates large-amplitude limit cycles that can substantially elevate the extinction risk [4–6]. This paradox of enrichment has remained one of the most discussed phenomena in population ecology for over five decades [7–9].

Real populations, however, are finite. Demographic stochasticity is the inherent randomness arising from discrete birth, death, and predation events in populations of finite size. This randomness ensures that the approach to a Hopf bifurcation is accompanied by growing fluctuations even while the deterministic equilibrium remains locally stable [10–12]. These noise-driven, quasi-periodic fluctuations are commonly termed quasi-cycles or stochastic amplification. They produce coherent oscillatory signatures in both time series and power spectra that can serve as early warning signals of an impending bifurcation [13, 14]. Detecting and interpreting such noisy precursors has practical relevance for ecosystem management and ecological modeling, where interventions must typically be made before the deterministic bifurcation point is actually crossed [15–17]. In predator–prey systems, demographic noise can be selectively amplified by the weakly damped linearized dynamics near coexistence. This amplification produces a nonzero-frequency spectral peak and visibly oscillatory time series before the deterministic Hopf threshold is crossed. In that sense, quasi-cycles are not merely a stochastic curiosity. Instead, they offer a practically relevant pre-bifurcation signature of reduced resilience. This also helps explain why empirical population records may exhibit a sustained oscillatory structure before deterministic instability sets in.

Linear noise approximation (LNA) provides the standard analytical bridge between the stochastic birth–death process and its continuous diffusion limit [18–20]. Within the LNA framework, fluctuations near a stable equilibrium are described by an Ornstein-Uhlenbeck (OU) process. The stationary covariance matrix of this process satisfies a continuous Lyapunov equation, and its spectral properties are encoded in a matrix-valued power spectral density (PSD) [21, 22]. As the Hopf threshold is approached, the resolvent of the linearized dynamics develops a resonance near the frequency of the incipient limit cycle. This resonance produces a characteristic spectral peak in the PSD, which sharpens and grows in amplitude [23, 24].

A key modeling choice concerns the covariance structure of the demographic noise. This choice is often made implicitly and forms the central focus of this paper. When a stochastic population model is derived from a continuous-time Markov chain (CTMC) or chemical master equation (CME) description of discrete events, the resulting equation is a stochastic differential equation (SDE). Its diffusion covariance then inherits the stoichiometric coupling of those discrete events [25–27]. In predator–prey systems, predation is mechanistically a coupled event: A single encounter simultaneously removes a prey individual and, with some probability, produces a predator offspring. Many stochastic analyses of ecological models, including influential studies of quasi-cycles, use diagonal (uncorrelated) or phenomenologically specified noise [28–30]. They effectively treat prey loss and predator gain as statistically independent channels.

Whether this modeling simplification fundamentally alters near-Hopf diagnostics in finite ecosystems has not been systematically examined quantitatively. This paper addresses that gap by rigorously benchmarking the effects of noise covariance against the inherent limitations of local linear approximations. To do so, we develop and compare two diffusion closures that share an identical R–M deterministic drift but differ precisely in their predation-induced covariance structure. We contrast a full-covariance model retaining the mechanistically inherited negative cross-covariance with a drift-matched diagonal noise comparator treating predation-related prey loss and predator gain as independent channels. The comparison is "fair" because the only modeling difference lies in the off-diagonal diffusion covariance. The deterministic dynamics, marginal noise intensities, and parameter values remain identical across the models.

We propagate the full non-diagonal local diffusion covariance through the entire LNA diagnostic chain, which includes stationary covariance, matrix PSD, and stochastic sensitivity function (SSF) confidence ellipses. Crucially, by benchmarking these analytical predictions against exact nonlinear CTMC simulations, the analysis reveals a surprising result. Near a Hopf bifurcation, the profound breakdown of the linear approximation eclipses the subtle geometric differences induced by the off-diagonal covariance.

Appendix A reviews the relevant literature, on which we based our research. The present paper integrates and extends several of the threads surveyed above. Our primary novelty lies in demonstrating that near a Hopf bifurcation in finite ecosystems, the breakdown of linear quasi-cycle theory and the resulting boundary-hitting risks outweigh the specific structural details of the demographic noise. Its contributions relative to the existing literature can be summarized as follows. First, we provide a systematic, "fair-comparison" framework in which the sole modeling variable is the predation-induced off-diagonal covariance, while all other model ingredients are kept fixed. Second, we propagate the full non-diagonal diffusion covariance through the complete LNA diagnostic chain. This chain includes the Lyapunov covariance, the matrix PSD, the SSF ellipse, and the noisy precursor indicator. We do not stop at the PSD level, which is a common limitation in the quasi-cycle literature. Third, we introduce the dimensionless noisy precursor indicator Π_p as a compact scalar diagnostic that synthesizes the fluctuation magnitude, geometry, and proximity to extinction boundaries. Finally, we provide quantitative evidence concerning the standard LNA framework. While LNA predicts unbounded spectral amplification and variance inflation near k_H, the true nonlinear CTMC dynamics remain strictly bounded and are instead systematically driven toward physical extinction boundaries. Taken together, these contributions clarify a key requirement for robust early warning inference. Such inference must account for nonlinear saturation and discrete population thresholds, rather than relying solely on the fine-scale mechanistic structure of the local noise.

Figure 1 provides a mechanistic overview of our work. It is organized as follows. Section 2 reviews the deterministic R–M model, its equilibria, and the enrichment-driven Hopf bifurcation. Section 3 defines the stochastic diffusion models used throughout the paper, with emphasis on the full-covariance and diagonal noise closures and the structural sign of the predation-induced cross-covariance. Section 4 discusses the open-domain and absorbed boundary viewpoints for interpretation. Section 5 develops the main analytical framework: LNA/OU reduction, Lyapunov covariance, matrix PSD, stochastic sensitivity ellipses, and the noisy precursor indicator. The appendices provide detailed derivations of the PSD (Appendix B) alongside the 2×2 Lyapunov solution and SSF formulas (Appendix C). They also contain explicit covariance closures (Appendix D), the Jacobian at the coexistence equilibrium

(Appendix E), and technical proofs for the covariance structure results (Appendix F).

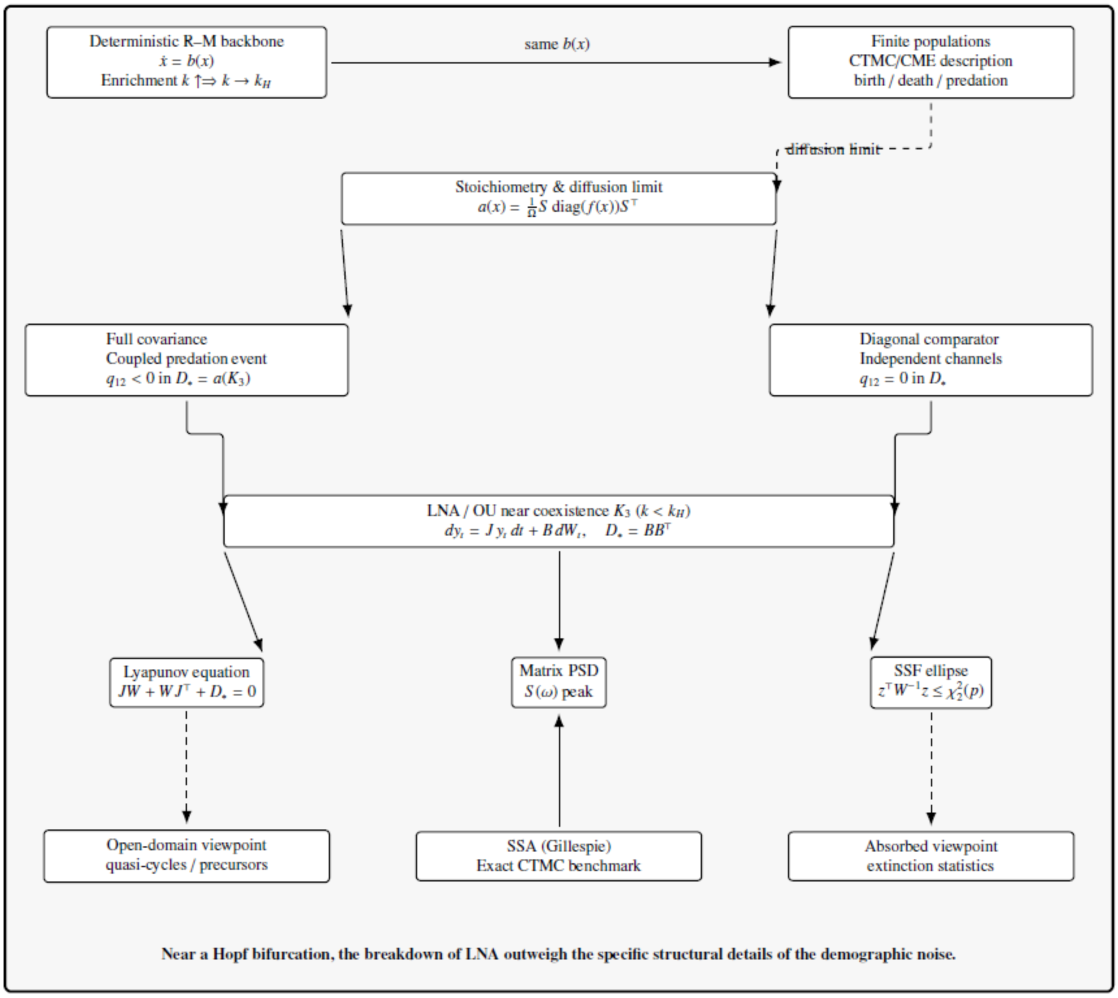

Figure 1. Mechanism overview. Environmental enrichment drives the deterministic backbone toward Hopf bifurcation. Stoichiometric coupling determines the diffusion covariance. Two drift-matched closures differ only in their off-diagonal covariance.

2. Deterministic R–M backbone and enrichment regimes

This section records the deterministic R–M structure used to organize the stochastic diagnostics developed later. We only retain the ingredients needed for the near-Hopf analysis: The nondimensional model, the coexistence equilibrium, its feasibility conditions, the enrichment-driven Hopf threshold, and the resulting parameter partition.

We consider the following nondimensional R–M predator–prey system with Holling Type II predation:

$$\begin{cases} \dfrac{dN}{dt} = N\left(1 - \dfrac{N}{k}\right) - \dfrac{mNP}{1+N}, \\ \dfrac{dP}{dt} = P\left(-c + \dfrac{mN}{1+N}\right), \end{cases} \qquad (N(t), P(t)) \in Q := \{(N, P) : N \ge 0,\ P \ge 0\}, \tag{2.1}$$

where N and P denote prey and predator densities, respectively. The parameter $k > 0$ is the (scaled) prey carrying capacity, $c > 0$ is the predator mortality parameter, and $m > 0$ is the maximal predation/assimilation parameter under the present nondimensionalization.

The biologically relevant state space is the non-negative quadrant Q, with the interior

$$D := (0, \infty)^2. \tag{2.2}$$

The stochastic diffusion models studied later will use the same state-space geometry, but with different boundary interpretations (open-domain versus absorbed viewpoints; Section 4).

For the coexistence equilibrium and feasibility, System (2.1) admits the boundary equilibria

$$K_1 = (0, 0), \qquad K_2 = (k, 0),$$

and the coexistence equilibrium

$$K_3 = (N^*, P^*) = \left(\frac{c}{m - c}, \ \frac{k(m - c) - c}{k(m - c)^2}\right). \tag{2.3}$$

The coexistence equilibrium K_3 lies in D if and only if

$$m > c \qquad \text{and} \qquad k(m - c) > c. \tag{2.4}$$

The condition $m > c$ ensures that predators' per-capita growth can become non-negative at a sufficiently high prey density, while $k(m - c) > c$ is exactly the positivity condition $P^* > 0$.

For the enrichment-driven Hopf threshold, linearization of (2.1) at K_3 yields the classical enrichment-driven Hopf threshold

$$k_H = \frac{m + c}{m - c}, \tag{2.5}$$

in the parameter regime where $K_3 \in D$. Thus, in the standard R–M setting, we have

$$k < k_H \ \Rightarrow \ K_3 \text{ is locally asymptotically stable}, \qquad k > k_H \ \Rightarrow \ K_3 \text{ is unstable},$$

with a Hopf bifurcation as k crosses k_H. This threshold is the deterministic backbone for the near-Hopf stochastic amplification and quasi-cycle diagnostics studied in this paper.

As a parameter partition for stochastic analysis, we use the Hopf threshold (2.5) to define the parameter regions

$$\begin{aligned} \Lambda_2 &:= \{(m, c, k) : k < k_H\} \quad \text{(deterministically stable coexistence regime)}, \\ \Lambda_1 &:= \{(m, c, k) : k > k_H\} \quad \text{(post-Hopf oscillatory regime)}. \end{aligned} \tag{2.6}$$

The present paper focuses primarily on Λ_2, especially parameter values with $k \uparrow k_H$, where deterministic coexistence remains stable but demographic noise can generate pronounced quasi-cycles and noisy precursors. The post-Hopf regime Λ_1 is included mainly for comparisons.

In this paper, the deterministic partition mainly serves as the organizing backbone for stochastic diagnostics.

3. Stochastic diffusion model and covariance structures

This section states the stochastic diffusion models used throughout the paper in a self-contained form, with emphasis on the covariance structures that drive the near-Hopf diagnostics. Our focus here is not to re-derive the full CTMC/CME construction in detail. Instead, we aim to provide reproducible model definitions for (i) a mechanistically consistent full-covariance demographic diffusion and (ii) a drift-matched diagonal noise comparator. The detailed calculations and proofs of the structural covariance results in this section are given in Appendix F.

In this paper, the two stochastic closures play distinct modeling roles. The full-covariance closure is the mechanistically faithful default because it preserves the same-event coupling inherent in predation. Specifically, a predation encounter removes prey and contributes to the predators' gain within the same microscopic event, which induces a negative prey–predator diffusion cross-covariance. By contrast, the diagonal noise comparator is not introduced as a more realistic ecological model, but as a deliberately simplified benchmark that suppresses this diffusion-level coupling while preserving the deterministic drift. Its purpose is therefore diagnostic rather than mechanistic: It allows us to isolate how much of the near-Hopf fluctuation structure is specifically attributable to covariance coupling rather than to the deterministic backbone.

For mechanistically derived demographic diffusion, let

$$x_t = (N_t, P_t)^\top \in \mathbb{R}_+^2$$

denote the prey and predator densities, and let $\Omega > 0$ be the system-size parameter (population scale). We use the density-level Itô SDE

$$dx_t = b(x_t)\,dt + \Sigma(x_t)\,dW_t, \tag{3.1}$$

where W_t is a standard Brownian motion (of a dimension determined by the chosen factorization), and the diffusion covariance is

$$a(x) := \Sigma(x)\Sigma(x)^\top = \frac{1}{\Omega} S\ \operatorname{diag}(f(x))\, S^\top. \tag{3.2}$$

Here, S is a stoichiometric matrix and $f(x)$ is a vector of density-level event intensities associated with a chosen mechanistic closure. Equation (3.2) is the key modeling identity: The diffusion covariance is inherited from event stoichiometry and channel intensities.

Throughout this paper, we use the reduced nondimensional R–M drift

$$b(x) = \begin{pmatrix} N\left(1 - \dfrac{N}{k}\right) - \dfrac{mNP}{1+N} \\ P\left(-c + \dfrac{mN}{1+N}\right) \end{pmatrix}, \qquad x = (N, P)^\top. \tag{3.3}$$

This is the same deterministic backbone as in Section 2. In the present paper, the stochastic modeling question is how different covariance structures $a(x)$ (with the same drift (3.3)) affect near-Hopf second-order diagnostics and agreement with SSA.

We compare two diffusion closures that share the same deterministic drift but differ in their predation-induced covariance structure. The full-covariance model, representing the mechanistic default, couples predation and predator conversion at the event level, resulting in a nonzero prey–predator noise cross-covariance $a_{12}(x)$, which is typically negative. In contrast, the diagonal noise comparator, serving as a drift-matched baseline, represents predation-related prey loss and predator gain via split channels, so that the covariance contribution is diagonal in the prey–predator block, while the deterministic drift and marginal predation intensities remain matched.

To make this explicit, we write

$$f_{\mathrm{pred}}(x) := \frac{mNP}{1+N}.$$

For notational continuity with the mechanistic derivation, we temporarily include a conversion efficiency $e \in (0, 1]$.

For the Bernoulli-coupled predation conversion mechanism, in which each predation encounter removes one prey and produces a predator offspring with probability e, the contribution of predation to the density diffusion covariance is

$$a^{(B)}_{\mathrm{pred}}(x) = \frac{1}{\Omega} f_{\mathrm{pred}}(x) \begin{pmatrix} 1 & -e \\ -e & e \end{pmatrix}. \tag{3.4}$$

This covariance is inherited directly from the exact Bernoulli-coupled integer-valued mechanism after diffusion approximation.

The effective coupled diffusion-level closure replaces the Bernoulli mechanism by a single effective predation channel with the stoichiometric increment $(-1, e)^\top$, resulting in

$$a^{(\mathrm{eff})}_{\mathrm{pred}}(x) = \frac{1}{\Omega} f_{\mathrm{pred}}(x) \begin{pmatrix} 1 & -e \\ -e & e^2 \end{pmatrix}. \tag{3.5}$$

This closure preserves the predation-induced cross-covariance sign and magnitude of (3.4), serving as a compact full-covariance representation.

Finally, in the split-channel diagonal noise comparator, predation-related prey removal and predator reproduction are treated as independent channels, while the deterministic drift and marginal predation intensities are matched. The resulting contribution of predation is

$$a^{(S)}_{\mathrm{pred}}(x) = \frac{1}{\Omega} f_{\mathrm{pred}}(x) \begin{pmatrix} 1 & 0 \\ 0 & e \end{pmatrix}, \tag{3.6}$$

which yields zero predation-induced cross-covariance between prey and predator.

In all three cases, the full diffusion covariance $a(x)$ is obtained by adding the contribution of predation to the common birth/competition/death contributions implied by (3.2). Thus the comparator is drift-matched and differs from the full-covariance model specifically in the second-order coupling structure. Figures 2 and 3 visualize the modeling distinctions between the full-covariance (A and B) and the baseline comparator (C) models.

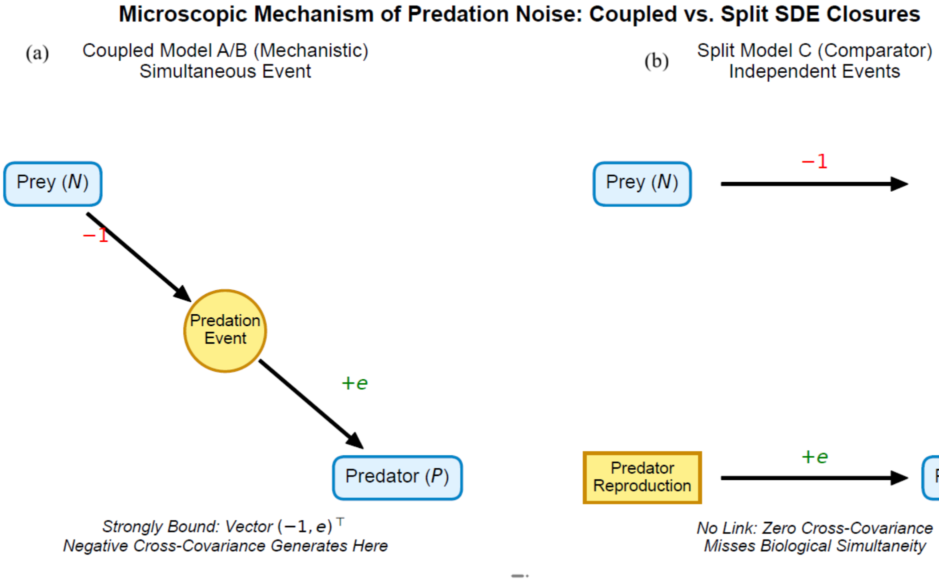

Figure 2. Microscopic mechanism of predation noise. (a) In the coupled closures, a single predation event simultaneously reduces prey and increases predator populations, generating a structurally negative cross-covariance. (b) In the split-channel comparator, these are treated as independent events, yielding zero cross-covariance despite matching the deterministic drift.

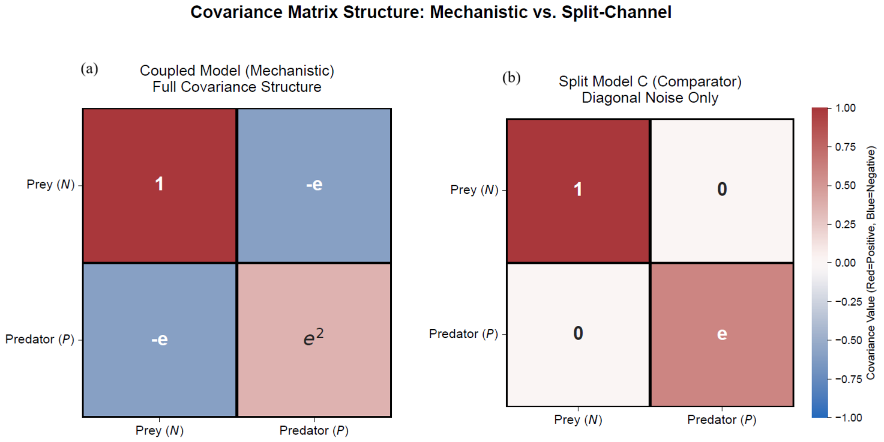

Figure 3. Covariance matrix structure. Heatmap representation of the contribution of predation to the diffusion covariance. The mechanistic full-covariance model (a) exhibits negative cross-covariance (blue), whereas the split-channel comparator (b) explicitly zeroes out this off-diagonal coupling (white), preserving only the diagonal variances (red).

For the structural predation-induced cross-covariance, the key covariance distinction used throughout the paper is summarized in the following observation.

Proposition 3.1 (Structural predation-induced cross-covariance)**.** *Under a coupled predation conversion closure (Bernoulli-coupled or effective* $(-1, e)^\top$ *closure), the contribution of predation to* *the diffusion covariance satisfies*

$$(a_{\mathrm{pred}})_{12}(x) < 0, \qquad x \in (0, \infty)^2. \tag{3.7}$$

In contrast, for the drift-matched split-channel comparator, we have

$$(a^{(S)}_{\mathrm{pred}})_{12}(x) = 0, \qquad x \in (0, \infty)^2. \tag{3.8}$$

Proof. From (3.4) and (3.5), we have

$$(a_{\mathrm{pred}})_{12}(x) = -\frac{1}{\Omega}\, e\, f_{\mathrm{pred}}(x) = -\frac{1}{\Omega}\, e\, \frac{mNP}{1+N} < 0 \quad \text{for } N, P > 0.$$

Equation (3.8) follows directly from (3.6). □

We fix $e = 1$. Only in this case, the Bernoulli-coupled and effective coupled closures coincide at the predation-covariance level:

$$a^{\mathrm{full}}_{\mathrm{pred}}(x) = \frac{1}{\Omega}\, f_{\mathrm{pred}}(x) \begin{pmatrix} 1 & -1 \\ -1 & 1 \end{pmatrix}, \qquad f_{\mathrm{pred}}(x) = \frac{mNP}{1+N}. \tag{3.9}$$

The superscript "full" represents "B" or "eff" in (3.4) and (3.5), depending on the context. Hence the full-covariance diffusion matrix is

$$a^{\mathrm{full}}(x) = a_0(x) + a^{\mathrm{full}}_{\mathrm{pred}}(x) = \frac{1}{\Omega} \begin{pmatrix} N + \dfrac{N^2}{k} + \dfrac{mNP}{1+N} & -\dfrac{mNP}{1+N} \\ -\dfrac{mNP}{1+N} & cP + \dfrac{mNP}{1+N} \end{pmatrix}. \tag{3.10}$$

The drift-matched diagonal noise comparator is

$$a^{\mathrm{diag}}(x) = a_0(x) + a^{(S)}_{\mathrm{pred}}(x)\Big|_{e=1} = \frac{1}{\Omega} \begin{pmatrix} N + \dfrac{N^2}{k} + \dfrac{mNP}{1+N} & 0 \\ 0 & cP + \dfrac{mNP}{1+N} \end{pmatrix}. \tag{3.11}$$

Comparing (3.10) and (3.11), the diagonal entries are identical, and the two models differ in their covariance structures. The full-covariance model and the diagonal comparator differ solely in that the off-diagonal covariance is only literally true after the specialization $e = 1$:

$$a^{\mathrm{full}}_{11}(x) = a^{\mathrm{diag}}_{11}(x) = N + \frac{N^2}{k} + \frac{mNP}{1+N}, \qquad a^{\mathrm{full}}_{22}(x) = a^{\mathrm{diag}}_{22}(x) = cP + \frac{mNP}{1+N}. \tag{3.12}$$

Proposition 3.1 provides the structural basis for the comparisons in later sections, because the LNA covariance, matrix PSD, and stochastic sensitivity ellipse all depend on the local diffusion covariance $D_* = a(K_3)$.

4. Open-domain and absorbed viewpoints for stochastic interpretation

The diffusion model in Section 3 can be used under two complementary global viewpoints, depending on whether the scientific objective is analyzing interior fluctuations or extinction-permitting dynamics. In this paper, this distinction is primarily interpretive and computational: We use it to align the model's formulation with the observable of interest, rather than to develop a full boundary well-posedness theory.

We first introduce the open-domain viewpoint for the interior dynamics and near-Hopf diagnostics. In this viewpoint, the diffusion is interpreted in the interior state space

$$D = (0, \infty)^2,$$

and is used to describe survival-conditioned or interior stochastic dynamics near the coexistence equilibrium K_3. This is the natural setting for the local analyses developed later in the paper, including LNA around K_3, stationary covariance (Lyapunov equation) in the Hurwitz regime, matrix PSD and quasi-cycle diagnostics, and SSF confidence ellipses and the noisy precursor indicator. These diagnostics characterize the fluctuation amplification and geometry before deterministic oscillatory onset, and they are inherently interior objects centered at the coexistence state. Related results have been obtained in epidemic systems [31], where the positivity and boundedness of globally exponentially stable periodic solutions were obtained.

We discuss the absorbed viewpoint for the extinction-permitting dynamics. In this viewpoint, the same local diffusion coefficients are used up to boundary contact, but the trajectories are treated as extinct (absorbed) once a boundary corresponding to the loss of coexistence is reached (i.e., $N = 0$ and/or $P = 0$). In our computational framework, the absorbed viewpoint is implemented by terminating the trajectory at its first time of hitting an extinction boundary; we do not continue the path as a one-dimensional boundary process. This viewpoint is the diffusion-level analog of the irreversibility present in the finite-population CTMC model, where extinction is absorbing in the absence of immigration or external forcing.

The absorbed viewpoint is therefore the appropriate choice when the target observables involve extinction-permitting behavior, such as absorption probabilities, survival curves, or qualitative comparisons of boundary-hitting tendencies with SSA trajectories. In the present paper, we use the absorbed diffusion viewpoint mainly to compare against SSA in finite-population regimes and to separate extinction-related effects from the interior fluctuation diagnostics obtained under the open-domain viewpoint.

In summary, using both viewpoints allows us to compare stochastic signatures across modeling levels while keeping the interpretation of each diagnostic aligned with the appropriate boundary treatment.

5. LNA near coexistence: Covariance, PSD, stochastic sensitivity, and noisy precursors

This section develops the main analytical diagnostics of the paper for stochastic fluctuations near the coexistence equilibrium K_3 in the deterministically stable regime Λ_2 (Section 2). The goal is to quantify how demographic noise is amplified as the enrichment-driven Hopf threshold is approached.

A key point of novelty is the explicit propagation of a mechanistically inherited non-diagonal local diffusion covariance $D_* = a(K_3)$ through the entire LNA diagnostic chain. In much of the quasi-cycle/LNA literature, noise is taken to be diagonal (or its covariance structure is not analyzed explicitly). In our model, the full-covariance model induces a prey–predator cross-covariance at the diffusion level, and this enters directly into the Lyapunov covariance, matrix PSD, and stochastic sensitivity (SSF) ellipse.

Throughout this section, we work with the open-domain viewpoint of Section 4 and the stochastic diffusion model of Section 3, with deterministic drift (3.3). The focus is local (near K_3) and applies to the deterministically stable coexistence regime Λ_2, especially near the Hopf threshold k_H.

For LNA / OU reduction around the coexistence equilibrium, we assume that the coexistence equilibrium

$$K_3 = (N^*, P^*)$$

exists in $D = (0, \infty)^2$ (Section 2). Let

$$J := J(K_3)$$

denote the Jacobian of the deterministic drift at K_3, and let

$$D_* := a(K_3) = \Sigma(K_3)\Sigma(K_3)^\top$$

be the local diffusion covariance matrix at K_3 for the chosen noise closure (full-covariance model or diagonal comparator).

Define the fluctuation variable

$$y_t := x_t - K_3.$$

Linearizing the drift around K_3 and freezing the diffusion covariance at K_3 yields the LNA, i.e., the OU SDE

$$dy_t = J\, y_t\, dt + B\, dW_t, \qquad BB^\top = D_*, \tag{5.1}$$

where B is any matrix factorization of D_*.

In the deterministically stable regime $\Lambda_2 = \{k < k_H\}$, the coexistence equilibrium K_3 is locally asymptotically stable, and hence J is Hurwitz (equivalently, in two dimensions, $\mathrm{tr}(J) < 0$ and $\det(J) > 0$). Therefore, the OU process (5.1) admits a unique stationary Gaussian distribution with a zero mean and the covariance matrix W.

The LNA is a local approximation centered at K_3 and is most informative in Λ_2 near k_H, where deterministic attraction persists but stochastic amplification is strong. In particular, the stationary covariance/PSD/SSF diagnostics developed below are defined only in the Hurwitz regime Λ_2. In the post-Hopf regime Λ_1, $J(K_3)$ is not Hurwitz and one should not impose a stationary OU interpretation around K_3.

For stationary covariance via the continuous Lyapunov equation. Let

$$W := \mathbb{E}[y_t y_t^\top]$$

denote the stationary covariance matrix of the OU process (5.1) (when J is Hurwitz). Then W is the unique symmetric positive definite solution of the continuous Lyapunov equation

$$JW + WJ^\top + D_* = 0. \tag{5.2}$$

This matrix equation is the central covariance object for the stochastic sensitivity analysis.

Since the R–M model is two-dimensional, write

$$J = \begin{pmatrix} \alpha & \beta \\ \gamma & \delta \end{pmatrix}, \qquad D_* = \begin{pmatrix} q_{11} & q_{12} \\ q_{12} & q_{22} \end{pmatrix}, \qquad W = \begin{pmatrix} w_{11} & w_{12} \\ w_{12} & w_{22} \end{pmatrix}.$$

Then (5.2) is equivalent to the 3×3 linear system

$$\begin{pmatrix} 2\alpha & 2\beta & 0 \\ \gamma & \alpha + \delta & \beta \\ 0 & 2\gamma & 2\delta \end{pmatrix} \begin{pmatrix} w_{11} \\ w_{12} \\ w_{22} \end{pmatrix} = - \begin{pmatrix} q_{11} \\ q_{12} \\ q_{22} \end{pmatrix}. \tag{5.3}$$

Hence W can be obtained by a robust linear solution (or by a standard Lyapunov solver). Appendix C gives the componentwise derivation and explicit 2×2 formulas.

Under the full-covariance stochastic model, $D_+ = a(K_3)$ is generally non-diagonal, reflecting mechanistic prey–predator coupling. Therefore, the stationary covariance W inherits not only the deterministic linearized dynamics J but also the noise geometry encoded in D_*. This is precisely where the full-covariance and diagonal noise models can quantitatively diverge even when they share the same drift.

The LNA/OU representation also yields a closed-form matrix-valued PSD, which makes the quasi-cycle amplification transparent in the frequency domain.

Let $S(\omega) \in \mathbb{C}^{2\times 2}$ denote the stationary matrix PSD of the OU process (5.1). Then

$$S(\omega) = (J - i\omega I)^{-1} D_* (J^\top + i\omega I)^{-1}, \qquad \omega \in \mathbb{R}. \tag{5.4}$$

A Fourier-domain derivation is given in Appendix B. The diagonal entries

$$S_{NN}(\omega), \qquad S_{PP}(\omega)$$

are the fluctuation spectra of the prey and predator, while the off-diagonal entries encode cross-spectral coupling and phase information. In Λ_2, especially for $k \uparrow k_H$, one typically observes the emergence and sharpening of a nonzero-frequency spectral peak (quasi-cycles), increased spectral amplification near the resonant frequency as $\mathrm{tr}(J) \uparrow 0$, and covariance structure dependence of the spectral matrix through D_*, not only through J. Thus the PSD provides a direct frequency-domain signature of noisy precursors before deterministic destabilization.

At the deterministic Hopf threshold, the real parts of the eigenvalues of J cross zero. In the stable regime Λ_2, the resolvent

$$(J - i\omega I)^{-1}$$

becomes increasingly amplifying near the imaginary part of the eigenvalues as $k \uparrow k_H$, producing the characteristic quasi-cycle spectral peak. The noise covariance D_* determines how strongly different fluctuation directions are injected into this amplified linear response.

Regarding stochastic sensitivity, confidence ellipses, and a noisy precursor indicator, the stationary covariance W obtained from (5.2) defines a local stochastic sensitivity geometry around K_3.

For a confidence level $p \in (0, 1)$, define the (deviation coordinate) confidence ellipse

$$\mathcal{E}_p := \left\{ z \in \mathbb{R}^2 : \ z^\top W^{-1} z \le \chi_2^2(p) \right\}, \tag{5.5}$$

where $\chi_2^2(p)$ is the p-quantile of the χ^2 distribution with two degrees of freedom. This is the SSF level set in the LNA/OU approximation.

Let $\lambda_\pm(W)$ be the eigenvalues of W, ordered such that $\lambda_+ \geq \lambda_- > 0$. Then the semi-axis lengths of $\mathcal{E}_p$ are

$$\ell_\pm = \sqrt{\chi_2^2(p)\,\lambda_\pm(W)}. \tag{5.6}$$

The principal-axis orientation is determined by the eigenvectors of W (equivalently, by the standard 2×2 angle formula; Appendix C).

In the full-covariance model (Model A/B in Section 3), the non-diagonal diffusion matrix D_* influences the stationary covariance W through the continuous Lyapunov equation (5.2). Importantly, because the Jacobian matrix J inherently couples the prey and predator dynamics, the stochastic sensitivity (SSF) ellipses for both the full-covariance model and the split-channel comparator (Model C) are fundamentally tilted relative to the coordinate axes. However, neglecting the negative off-diagonal cross-covariance in D_* (as in Model C) alters the exact orientation, eccentricity, and area of the covariance ellipse. Thus, even if a diagonal noise comparator matches the deterministic drift, it still introduces quantitative deviations in the true fluctuation geometry and anisotropy shaped by event-level demographic mechanisms. As shown by the solid blue ellipse in Figure 4, the full-covariance model produces a tilted fluctuation geometry that reflects diffusion-level prey–predator coupling. By contrast, the dashed green ellipse corresponding to the diagonal noise comparator removes the diffusion cross-covariance. However, the stationary ellipse may still remain rotated, because its orientation is determined jointly by J and D_* through the Lyapunov equation.

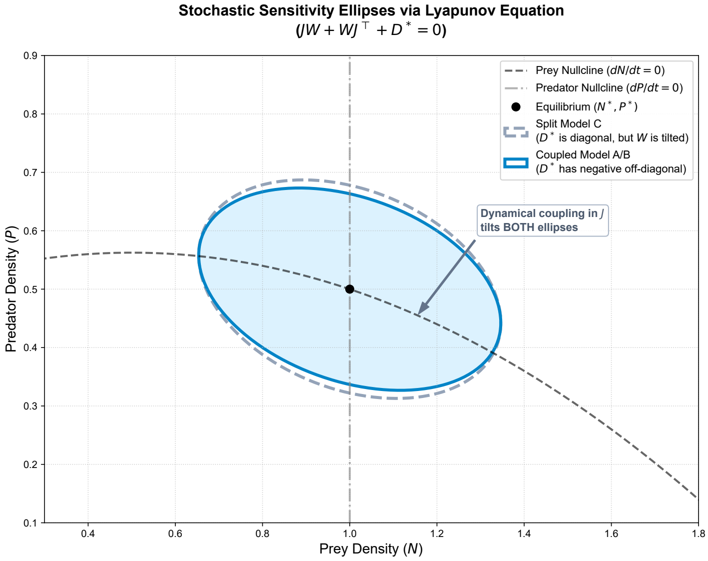

Figure 4. Stochastic sensitivity ellipses at the coexistence equilibrium. Both the full-covariance model (coupled Model A/B) and the split-channel comparator (split Model C) produce tilted covariance ellipses due to the inherent dynamical coupling in the Jacobian matrix J. However, the full-covariance model accurately incorporates a negative prey–predator diffusion cross-covariance induced by the simultaneous predation mechanism. Neglecting this off-diagonal diffusion term in the split-channel comparator leads to deviations in the exact orientation, eccentricity, and overall anisotropy of the fluctuation geometry.

To quantify how close typical fluctuations are to an extinction event, we operationally define the critical set $\mathcal{S}$ as the nearest extinction boundary. For the R–M model examples presented here, given the coexistence equilibrium $K_3 = (N^*, P^*)$, the physical extinction boundaries correspond to $N = 0$ and $P = 0$. Therefore,

$$\mathcal{S} := \{(N, P) \in \mathbb{R}^2_+ : N = 0 \text{ or } P = 0\},$$

and we define the separation distance d_{sep} as the Euclidean distance from K_3 to the nearest extinction boundary as follows

$$d_{\text{sep}} := \min\{N^*, P^*\}.$$

We explicitly acknowledge that this Euclidean distance serves as a local proxy rather than a global extinction risk formula. The local OU ellipse, derived from LNA, is an appropriate proxy for the boundary-hitting risk because it captures the intrinsic anisotropy and covariance structure of demographic fluctuations near the coexistence state. Specifically, the orientation and magnitude of the ellipse's semi-major axis (ℓ_+) encode the system's directional vulnerability, which reveals how strongly the predator–prey interaction stretches typical stochastic excursions toward the axes. Comparing this dominant directional stretch (ℓ_+) to the separation distance (d_{sep}) provides a physically meaningful, dimensionless indicator of the propensity for noise to drive the system across the extinction threshold:

$$\Pi_p := \frac{\ell_+}{d_{\text{sep}}}. \tag{5.7}$$

The interpretations using this indicator include typical fluctuations that remain well inside a local safe neighborhood ($\Pi_p \ll 1$); the noisy precursor regime, where confidence-level fluctuations are stretched enough to reach the nearest extinction boundary ($\Pi_p \approx 1$); and substantial noise-driven excursions toward extinction become plausible despite deterministic local stability ($k < k_H$) ($\Pi_p > 1$).

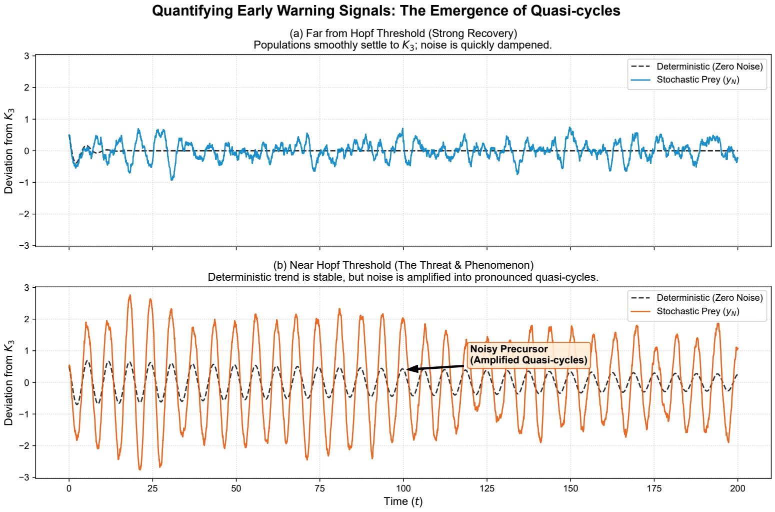

Figure 5. Emergence of noise-induced quasi-cycles near the Hopf bifurcation threshold. (a) System far from the Hopf threshold, exhibiting deterministic-dominated exponential decay toward the steady state. (b) System near the Hopf threshold, where demographic noise is amplified into pronounced quasi-cycles, serving as a noisy precursor to the bifurcation.

To illustrate this effect, Figure 5 compares the system's temporal evolution at different distances from the bifurcation. Far from the Hopf threshold (Panel a), the dynamics are dominated by deterministic decay to the steady state. In contrast, near the Hopf threshold (Panel b), demographic noise is dramatically amplified, generating sustained quasi-cycles prior to the actual bifurcation.

6. Numerical validation and reproducible benchmarks

This section provides the systematic numerical study requested to validate the analytical framework. We compare three modeling levels across a range of enrichment parameters approaching the Hopf threshold. The three levels include exact SSA (Gillespie's algorithm for the integer-valued CTMC), Euler–Maruyama integration of the full-covariance diffusion, and the drift-matched diagonal noise comparator.

6.1. Parameter values, simulation protocol, and reproducibility

All experiments use the nondimensional R–M models (2.1)–(3.1) with the parameter values in Table 1.

Table 1. Parameter values used in the numerical experiments.

Symbol	Value(s)	Description
m	1.5	Maximal predation/assimilation rate
c	0.5	Predator mortality rate
k_H	2.0	Hopf threshold = $(m+c)/(m-c)$
k	1.4, 1.6, 1.8, 1.9, 1.95, 1.98, 1.99	Carrying capacity (pre-Hopf, Λ_2)
k	2.2	Carrying capacity (post-Hopf, Λ_1)
Ω	500, 1000, 2000	System-size parameter
e	1	Conversion efficiency (fixed)
p	0.95	Confidence level for SSF ellipses
T_{sim}	200	Total simulation horizon
T_{burn}	50	Burn-in (discarded)
Δt	10^{-2}	Euler–Maruyama step size
Δt_{sample}	0.1	Sampling interval for PSD estimation
N_{MC}	200	Monte Carlo realizations per condition
n_{seg}	42	Welch PSD segment length

At $m = 1.5$ and $c = 0.5$, the coexistence equilibrium (2.3) is

$$K_3 = (N^*, P^*) = \left(\frac{c}{m-c},\ \frac{k(m-c)-c}{k(m-c)^2}\right) = \left(0.5,\ \frac{k-0.5}{k}\right).$$

For example, at $k = 1.9$, $K_3 \approx (0.5,\ 0.7368)$.

The exact Gillespie algorithm operates on integer-valued states (n, p) with the densities $(N, P) = (n/\Omega,\ p/\Omega)$. With $e = 1$, the dynamics comprise four event channels: prey birth at a rate n with the update $n \to n+1$; prey competition at a rate $n^2/(k\,\Omega)$ with the update $n \to n-1$; coupled predation conversion at a rate $m\,n\,p\,/(\Omega(1+n/\Omega))$ with the update $n \to n-1$ and $p \to p+1$; and predator death at a rate $c\,p$ with the update $p \to p-1$. The coupled predation conversion is a single coupled event and is not split into separate channels, so the SSA exactly preserves the Bernoulli-coupled event structure. Trajectories are initialized at the integer state nearest to $K_3 \cdot \Omega$ and terminated at absorption ($n = 0$ or $p = 0$) or at T_{sim}.

The density-level SDE (3.1) is integrated with the step $\Delta t = 10^{-2}$ using a Cholesky factorization of the local diffusion matrix $a(x)$ at each step. For the full-covariance model, $a(x) = a^{\text{full}}(x)$ as in (3.10); for the diagonal comparator, $a(x) = a^{\text{diag}}(x)$ as in (3.11). Densities are reflected at zero to implement the open-domain viewpoint (Section 4); the absorbed viewpoint is implemented by halting the trajectory at the first boundary contact.

Welch's method is applied to the post-burn-in segments of each realization, then averaged across the N_{MC} ensemble.

All simulations use the Python code with documented seeds. The complete simulation code is available at https://github.com/Louis-shuo-wang/The-Breakdown-of-Linear-Quasi-Cycles-Demographic-Noise-and-Absorbing-Boundaries-in-Finite-Systems.git.

6.2. *Parameter sweep: LNA diagnostics as $k \uparrow k_H$*

Figure 6 shows the LNA diagnostics for both noise closures as k traverses [1.2, 1.99] at a system size of $\Omega = 1000$. Four quantities are tracked: The noisy precursor indicator Π_p, the peak height of the prey PSD $S_{NN}(\omega)$, the dominant SSF semi-axis ℓ_+, and the SSF ellipse orientation angle.

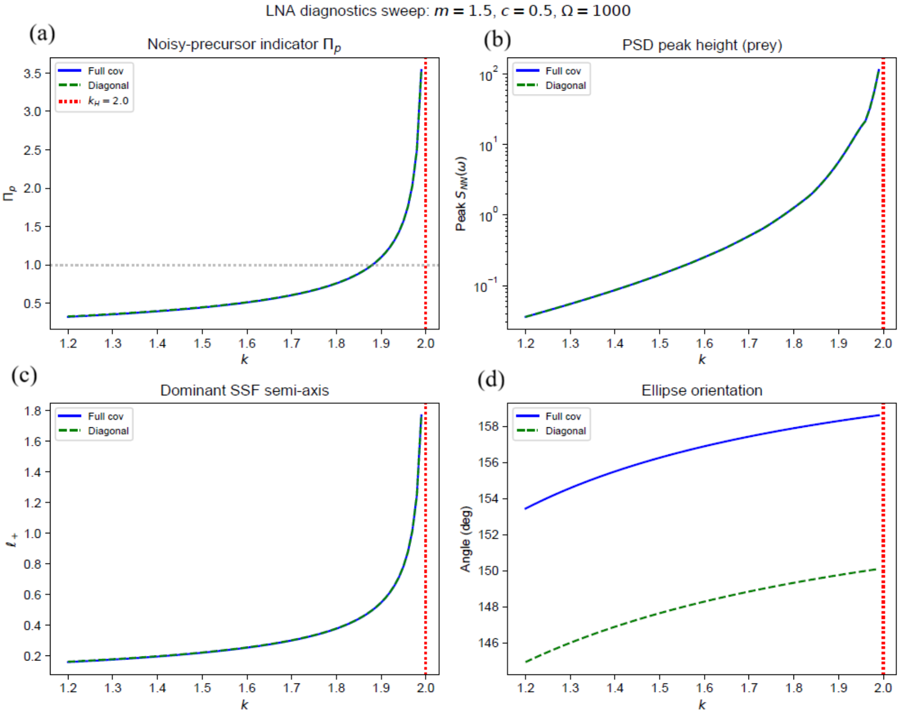

Figure 6. LNA diagnostic sweep as $k \uparrow k_H$. (a) noisy precursor indicator Π_p. (b) Prey PSD peak height (log scale). (c) Dominant SSF semi-axis ℓ_+. (d) Ellipse orientation angle. Blue solid line: Full-covariance model. Green dashed line: Diagonal comparator. Red dotted line: Hopf threshold $k_H = 2.0$. Parameters: $m = 1.5$, $c = 0.5$, $\Omega = 1000$; confidence level $p = 0.95$.

In stark contrast to potential expectations of large-magnitude deviations, the quantitative comparison reveals a striking finding. The magnitude-based diagnostics—the precursor indicator Π_p (Panel a), the PSD peak height (Panel b), and the dominant SSF semi-axis ℓ_+ (Panel c)—exhibit near-perfect agreement between the full-covariance and diagonal noise models across the entire parameter sweep. The differences in these scalar magnitude metrics are visually negligible. This indicates that for this specific parameter set ($m = 1.5$, $c = 0.5$), the off-diagonal diffusion covariance does not significantly alter the overall amplitude or the onset point ($\Pi_p = 1$) of the pre-bifurcation fluctuations.

However, the spatial geometry of the fluctuations is distinctly affected by the cross-covariance. The SSF ellipse orientation (Panel d) displays a persistent quantitative offset between the two closures. Throughout the sweep $k \in [1.2, 1.99]$, the full-covariance model predicts an ellipse tilted by approximately 153°–158°, while the diagonal comparator yields an angle that is consistently about 8° lower (ranging from roughly 145° to 149°). This robust geometric difference confirms that the magnitude of near-Hopf amplification is dominated by the diagonal noise's intensities. However, the precise fluctuation geometry—and thus the correlation structure between prey and predator—is distinctly shaped by the exact off-diagonal diffusion covariance channels.

6.3. SSA benchmarking: Covariance and PSD

Figure 7 compares the sample covariance matrix entries (W_{11}, W_{12}, W_{22}) obtained from SSA, full-covariance empirical Monte Carlo (EM), diagonal EM, and the corresponding LNA predictions, at $k \in \{1.6,\ 1.9,\ 1.99\}$ and $\Omega = 1000$.

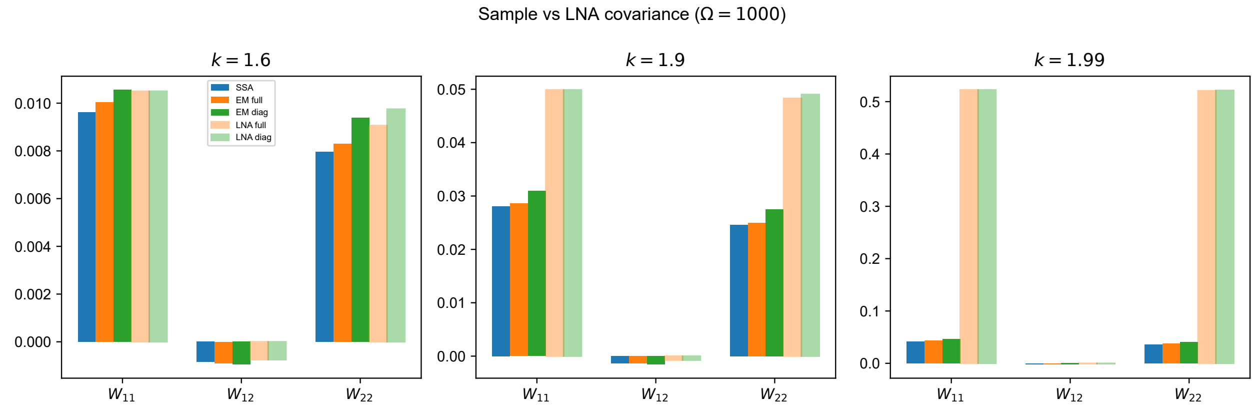

Figure 7. Sample covariance comparison. Grouped bar charts of W_{11}, W_{12}, W_{22} at three values of k (panels). Bars: SSA (blue), full-covariance EM (orange), diagonal EM (green), LNA full (light orange), LNA diagonal (light green). Parameters: $m = 1.5$, $c = 0.5$, $\Omega = 1000$, $N_{\mathrm{MC}} = 200$, $T_{\mathrm{sim}} = 200.0$.

At $k = 1.6$ (far from the Hopf bifurcation), all three nonlinear simulation methods (exact SSA, full-covariance EM, and diagonal EM) agree closely with the LNA's analytical predictions. In this regime, the differences between the full-covariance and diagonal noise closures are visually negligible across all matrix entries.

As k increases towards the Hopf threshold ($k_H = 2.0$), a distinct and systematic divergence occurs.

It is not between the different noise closures, but between the analytical LNA framework and the empirical nonlinear simulations. At $k = 1.9$ and, more dramatically, at $k = 1.99$, the three simulation methods (SSA, full EM, and diagonal EM) remain in remarkably close agreement with one another, demonstrating that the true system fluctuations are bounded. Similarly, the full and diagonal LNA predictions align closely with each other.

However, the gap between the simulation group and the LNA group widens significantly. Because the LNA relies on linearizing the drift, it predicts massive, asymptotically unbounded variance amplification as $k \uparrow k_H$. In contrast, the exact SSA and EM simulations naturally capture the nonlinear saturation effects that strictly constrain the true fluctuation magnitudes. Consequently, in the extremely near-Hopf regime, the breakdown of the linearization completely dominates the variance magnitudes, rendering the subtle differences induced by the specific off-diagonal noise structures marginal by comparison.

Figure 8 shows the ensemble-averaged prey PSD $S_{NN}(\omega)$ for the same parameter combinations, overlaid with the LNA's analytical predictions.

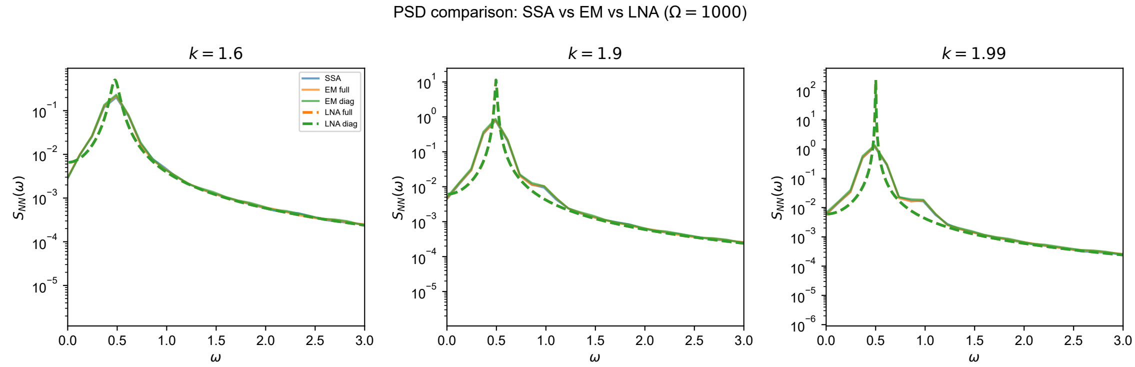

Figure 8. PSD comparison: SSA vs. EM vs. LNA. Prey PSD $S_{NN}(\omega)$ at $k \in \{1.6, 1.9, 1.99\}$. Solid curves: Empirical Welch PSD (SSA, EM full, EM diagonal). Dashed curves: LNA analytical PSD (LNA full, LNA diagonal). Parameters: $m = 1.5$, $c = 0.5$, $\Omega = 1000$, $N_{\mathrm{MC}} = 200$, $T_{\mathrm{sim}} = 200.0$.

Consistent with the covariance results, at $k = 1.6$ (far from the bifurcation), the analytical LNA accurately captures the exact empirical power spectrum across all frequencies. However, as the system approaches the Hopf threshold ($k = 1.9$ and $k = 1.99$), a profound divergence emerges between the linear theoretical predictions and the true nonlinear dynamics.

Contrary to the linear expectation, the exact SSA spectral peak does not align with the LNA predictions near k_H. Instead, both the full-covariance and diagonal LNA massively overestimate the peak height at the quasi-cycle frequency. At $k = 1.99$, the LNA predicts a resonant peak roughly two orders of magnitude higher than the true system response. This discrepancy fundamentally arises because the LNA lacks the nonlinear damping and saturation mechanisms that strictly constrain the amplitude of quasi-cycles in the true CTMC.

Concurrently, the empirical PSDs obtained from the SSA, full-covariance EM, and diagonal EM models remain in remarkably tight agreement with one another, all exhibiting properly bounded spectral peaks. This confirms that near the bifurcation, the massive breakdown of the linear approximation eclipses the subtle differences induced by the off-diagonal noise-injection geometry.

6.4. *SSF ellipses with SSA overlay*

Figure 9 shows the $p = 0.95$ SSF ellipses (full-covariance: solid blue; diagonal: dashed green) at $k = 1.9$ and $\Omega = 1000$, overlaid on a scatter of SSA trajectory points sampled after burn-in.

Contrary to the expectation of large macroscopic geometric differences, the full-covariance and diagonal comparator ellipses almost perfectly overlap at this system scale. Both noise closures yield nearly identical major and minor axes, successfully capturing the primary orientation and variance magnitude of the central SSA data cloud. It is worth noting that the true SSA scatter exhibits a mild crescent-like curvature indicative of intrinsic nonlinearities, which the strictly Gaussian SSF ellipses naturally approximate as a symmetric linear spread.

More importantly, the Figure 9 vividly illustrates the breakdown of the interior-fluctuation assumption. At $k = 1.9$, the massive near-Hopf noise resonance amplifies the covariance to such an extent that the $p = 0.95$ confidence ellipses forcefully cross the $N = 0$ axis into the unphysical negative-density domain. This geometric intersection visually corroborates the noisy precursor indicator ($\Pi_p > 1$) discussed earlier: The fluctuations have grown large enough that the CTMC has a high probability of hitting the biological extinction boundaries. Thus, rather than purely sustaining interior quasi-cycles, the resonant noise injection systematically drives the system toward an absorbing state.

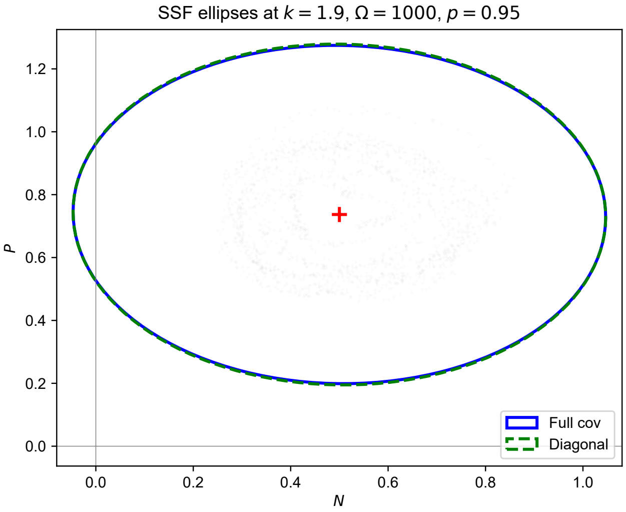

Figure 9. SSF ellipses overlaid on SSA scatter. Gray dots: SSA trajectory in (N, P)-space after burn-in. Blue solid line: full-covariance $p = 0.95$ ellipse. Green dashed line: diagonal comparator ellipse. Red cross: coexistence equilibrium K_3. $k = 1.9$, $\Omega = 1000$.

6.5. *System size sensitivity*

Figure 10 displays the $p = 0.95$ SSF confidence ellipses at a near-Hopf parameter ($k = 1.9$) across three different system sizes: $\Omega \in \{500, 1000, 2000\}$. As analytically expected from the LNA framework, the overall spatial extent of the fluctuation ellipses shrinks as the system's size increases, reflecting the $D_* \propto 1/\Omega$ scaling of the noise intensity.

Consistent with our previous geometric diagnostics, the full-covariance (solid blue) and diagonal comparator (dashed green) ellipses exhibit near-perfect overlap across all three panels. The expected orientation offset and eccentricity differences between the two closures are visually negligible at these macroscopic population scales. Instead, both models identically capture the dominant variance directions and magnitudes.

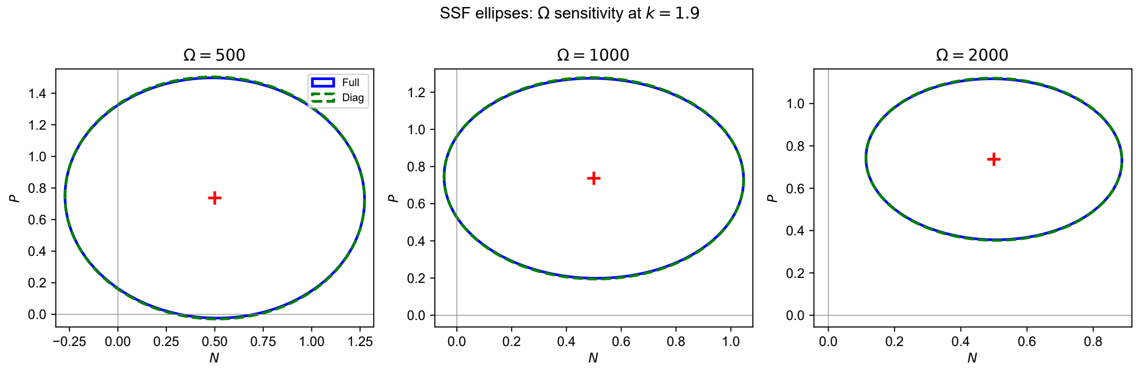

Figure 10. Ω sensitivity of SSF ellipses. Panels show the $p = 0.95$ confidence ellipses at $\Omega = 500$ (left), 1000 (center), and 2000 (right). Blue solid curves: full-covariance model. Green dashed curves: diagonal comparator. Red crosses mark the coexistence equilibrium K_3. Parameters: $k = 1.9$, $m = 1.5$, $c = 0.5$.

More profoundly, the scaling of the ellipse size vividly illustrates the critical role of Ω in mediating the boundary absorption risk. At smaller system sizes ($\Omega = 500$ and $\Omega = 1000$), the near-Hopf noise amplification is so severe that the fluctuation geometry forcefully intersects the unphysical $N \leq 0$ domain. This clearly signals a breakdown of the interior CTMC approximation and a severe risk of noise-induced extinction. In contrast, at the largest system size ($\Omega = 2000$), the intrinsic noise is sufficiently dampened such that the $p = 0.95$ ellipse remains strictly within the biologically feasible positive quadrant. This elegantly demonstrates how a sufficiently large population scale (Ω) can confine the resonant near-Hopf fluctuations, thereby rescuing the system from boundary absorption and restoring the validity of the interior quasi-cycle regime.

6.6. *Open-domain versus absorbed viewpoint: A concrete comparison*

To explicitly illustrate the distinction between the open-domain and absorbed-boundary viewpoints (Section 4), we present a single, representative stochastic trajectory. This demonstrates why relying solely on open-domain approximations is ecologically problematic near the Hopf bifurcation.

Figure 11 tracks the prey density $N(t)$ for the full-covariance SDE under identical noise increments but distinct boundary conditions ($k = 1.98$, $\Omega = 50$). The key distinction is the treatment of the discrete extinction threshold, $1/\Omega$, representing one individual.

Figure 11(a) shows the continuous open-domain viewpoint. Allowed to freely fluctuate, a severe noise-driven excursion pushes the density far below $1/\Omega$. Rather than terminating, the boundary reflection mathematically "rescues" the trajectory, generating persistent quasi-cycles. This reflects the standard LNA framework, which assumes indefinite support on $(0, \infty)^2$.

Figure 11(b) enforces the absorbed boundary viewpoint (the CTMC reality): Dropping below $1/\Omega$ triggers physical extinction, permanently clamping the state to zero. This reveals that what appeared to be a "large cycle" in the open domain is actually a fatal boundary crash.

Ultimately, internal quasi-cycle metrics (PSD peak, local covariance) accurately describe the noise geometry only when they are far from absorbing manifolds. As $k \uparrow k_H$, covariance inflation inevitably forces the trajectory across the $1/\Omega$ threshold. Here, open-domain predictions fail, and the boundary-hitting risk (Π_p) becomes the dominant biological reality.

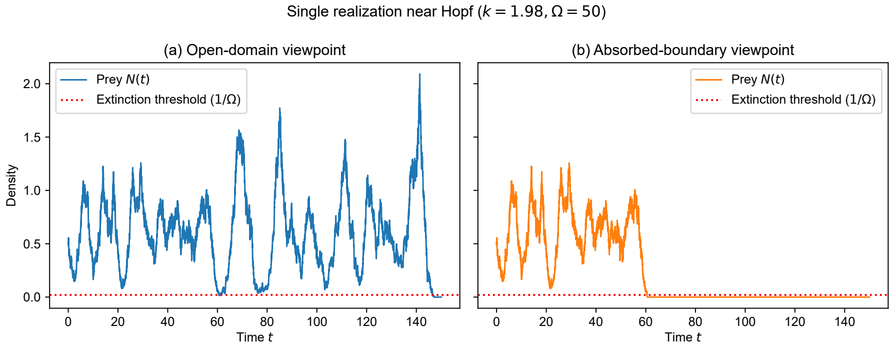

Figure 11. Concrete comparison of boundary viewpoints. Both panels depict the prey density $N(t)$ driven by identical Wiener noise increments. (a) Open domain viewpoint: The trajectory dips below the discrete extinction threshold ($1/\Omega$, red dotted line) but mathematically recovers, simulating persistent cycles. (b) Absorbed boundary viewpoint: The trajectory is absorbed at 0 upon crossing the physical $1/\Omega$ threshold, reflecting true CTMC extinction. Parameters: $k = 1.98$, $\Omega = 50$, $m = 1.5$, $c = 0.5$.

6.7. Quantitative error metrics

Table 2 reports the absolute errors between the analytical LNA predictions and EM estimates for the stationary covariance entries.

Table 2. Absolute errors $|W_{ij}^{\mathrm{LNA}} - W_{ij}^{\mathrm{EM}}|$ for selected k values ($\Omega = 1000$, $N_{\mathrm{MC}} = 200$). Values are rounded to four significant digits. FC = full-covariance, Diag = diagonal comparator.

	FC: LNA vs. EM			Diag: LNA vs. EM		
k	$\lvert\Delta W_{11}\rvert$	$\lvert\Delta W_{12}\rvert$	$\lvert\Delta W_{22}\rvert$	$\lvert\Delta W_{11}\rvert$	$\lvert\Delta W_{12}\rvert$	$\lvert\Delta W_{22}\rvert$
1.6	4.542×10^{-4}	1.417×10^{-4}	7.567×10^{-4}	5.460×10^{-5}	1.989×10^{-4}	3.670×10^{-4}
1.9	2.127×10^{-2}	6.317×10^{-4}	2.331×10^{-2}	1.893×10^{-2}	8.084×10^{-4}	2.151×10^{-2}
1.99	4.793×10^{-1}	1.117×10^{-3}	4.833×10^{-1}	4.756×10^{-1}	1.408×10^{-3}	4.805×10^{-1}

Consistent with our previous visual diagnostics at $k = 1.6$ (far from the bifurcation), both the full covariance and diagonal LNA models exhibit excellent agreement with their respective nonlinear EM simulations. The absolute errors remain negligible, strictly on the order of 10^{-4} or smaller across all matrix entries.

However, as the system approaches the Hopf threshold ($k = 1.9$ and $k = 1.99$), the absolute errors increase by several orders of magnitude. At $k = 1.99$, the discrepancy for the diagonal variance terms (W_{11} and W_{22}) reaches approximately 0.48. Crucially, this massive error inflation occurs almost symmetrically for both the full-covariance and the diagonal models. This quantitative result definitively confirms that the growing deviation is not an artifact of the specific noise-injection geometry (full vs.

diagonal), but rather stems directly from the fundamental breakdown of the LNA itself. Near k_H, the linear approximation inherently overpredicts the unbounded variance inflation, whereas the true nonlinear CTMC remains strictly bounded, resulting in the large absolute deviations tabulated below.

6.8. Operational definition of the noisy precursor indicator

Let $K_3 = (N^*, P^*)$ be the coexistence equilibrium in $D = (0, \infty)^2$. Recall that

$$\mathcal{S} := \{(N, P) \in \mathbb{R}^2_+ : N = 0 \text{ or } P = 0\}.$$

is the critical set. The separation distance is the Euclidean distance from K_3 to $\mathcal{S}$:

$$d_{\text{sep}} := \min\{N^*,\ P^*\}.$$

The dominant SSF semi-axis is

$$\ell_+ = \sqrt{\chi^2_2(p)\,\lambda_+(W)},$$

where $\lambda_+(W)$ is the largest eigenvalue of the stationary covariance W solving (5.2), and $\chi^2_2(p)$ is the p-quantile of the χ^2 distribution with two degrees of freedom. The noisy precursor indicator is

$$\Pi_p := \frac{\ell_+}{d_{\text{sep}}}.$$

We report the numerical values. At $m = 1.5$, $c = 0.5$, $\Omega = 1000$, $p = 0.95$: For $k = 1.6$, $K_3 = (0.5,\ 0.6875)$, $d_{\text{sep}} = 0.5$; for $k = 1.9$, $K_3 = (0.5,\ 0.7368)$, $d_{\text{sep}} = 0.5$; for $k = 1.99$, $K_3 = (0.5,\ 0.7487)$, $d_{\text{sep}} = 0.5$. The corresponding Π_p values are plotted in Figure 6(a).

7. Discussion and conclusions

This work clarifies a subtle but practically consequential point for stochastic ecological modeling near enrichment-driven Hopf bifurcations: Matching the deterministic drift does not guarantee matching the second-order stochastic diagnostics. Starting from a CTMC/CME description of discrete birth–death–predation events, we derived a mechanistically consistent diffusion approximation whose tensor inherits stoichiometric coupling. In the R–M modeling setting, predation is a same-event coupling between prey loss and (probabilistic) predator gain, which induces a structurally negative prey–predator cross-covariance in the local diffusion matrix. We contrasted this full-covariance closure with a drift-matched diagonal noise comparator. This comparator splits predation-related channels and therefore removes the off-diagonal term, while preserving the deterministic backbone and marginal noise intensities.

Our model revealed systematic differences in near-Hopf behavior. In the stable coexistence regime ($k < k_H$), the OU reduction shows that the stationary covariance, matrix-valued PSD, and stochastic sensitivity ellipses depend explicitly on the local diffusion covariance $D_* = a(K_3)$, not just on the Jacobian $J(K_3)$. However, our exact nonlinear benchmarking reveals a crucial reversal: As the system approaches the Hopf bifurcation, the macroscopic differences induced by the specific off-diagonal covariance structure become practically negligible. Instead, the dominant phenomenon is the fundamental breakdown of the local linear approximation itself. While the LNA erroneously predicts unbounded variance inflation and spectral amplification near k_H, the true CTMC dynamics remain constrained by nonlinear saturation. The dimensionless noisy precursor indicator Π_p further synthesizes these effects by comparing the dominant SSF semi-axis to an extinction-relevant distance scale. This comparison makes it explicit that near-Hopf fluctuation inflation inevitably forces the finite system into discrete absorbing boundaries (e.g., the $1/\Omega$ physical threshold) well before deterministic stability is formally lost.

From an applied ecological perspective, demographic stochasticity can affect population dynamics in several concrete ways. First, it can transform weakly damped return-to-equilibrium dynamics into clearly oscillatory population trajectories in finite systems. Second, it can broaden the cloud of fluctuations around coexistence, thereby increasing the frequency of excursions toward low-abundance, extinction-relevant regions. Third, it can alter the observed covariance geometry and spectral peak structure of population time series, which matters when one tries to infer resilience loss or an impending regime change from noisy ecological data. These effects are especially pronounced near the enrichment-driven Hopf threshold, where deterministic attraction is weak but stochastic amplification is strong.

Overall, our main conclusion is that nonlinear saturation and discrete boundary-hitting risks—rather than the fine-scale structural details of local noise covariance—are the true first-order modeling ingredients for pre-bifurcation inference in finite ecosystems. While stoichiometrically exact diffusions accurately capture baseline fluctuations far from the bifurcation, relying solely on linear open-domain approximations (like the LNA) near a Hopf threshold leads to severe overestimations of quasi-cycle amplitudes, blinding us to the biological reality of noise-induced extinction. Methodologically, the paper integrates bifurcation theory with mechanistic diffusion approximations and matrix-valued LNA tools (Lyapunov covariance, PSD, SSF) to provide a controlled, fair comparison template for assessing noise structure effects. Substantively, it strengthens the case for evaluating stochastic pre-bifurcation signals through the lens of absorbed boundary CTMC dynamics, rather than purely interior Gaussian fluctuations. A natural next step is to extend the present framework of nonlinear stochastic evaluation and boundary absorption to spatially extended predator–prey systems and structured PDE models. In such systems, mechanistic noise and demographic discreteness may interact with dispersal, pattern formation, or the internal-state structure to reshape the fluctuation geometry across both space and time.

Use of AI tools declaration

During the preparation of this work, the authors used Gemini 3 to conduct refine language. These contents were reviewed and edited by the authors to ensure accuracy.

Acknowledgments

The author Jiguang Yu gratefully acknowledges the support from his Distinguished PhD Fellowship from Boston University College of Engineering during the completion of this research. The research of Louis Shuo Wang is partially supported by the National Natural Science Foundation of China and the Tianyuan Fund for Mathematics (Project No. 12426516). This article was written while these authors were visiting the Tianyuan Mathematical Centre in Central China (Hubei).

Conflict of interest

The authors declare there are no conflicts of interest.

Appendix

A. Literature review

We briefly discuss the general literature and focus on four topics in this part: (i) The paradox of enrichment, (ii) demographic noise and the associated CME framework, (iii) quasi-cycles, and (iv) early warning signals. These are the broad topics on which we based our research.

A.1. The paradox of enrichment and Hopf bifurcations in predator–prey models

The theoretical prediction that nutrient enrichment can destabilize predator–prey coexistence dates to the seminal work of Rosenzweig [3]. He showed that increasing carrying capacity pushes the interior equilibrium through a Hopf bifurcation, triggering limit-cycle oscillations of growing amplitude. This observation, termed the paradox of enrichment, was formalized within the R–M model [32, 33], whose Type II functional response provides the minimal mechanistic skeleton needed to produce the bifurcation. Subsequent analytical studies established the supercritical character of the Hopf bifurcation [34, 35], while Bazykin [36] explored additional codimension-two degeneracies and global bifurcation structures in enriched predator–prey systems. Related stability and threshold analyses for feedback-regulated structured population models (including nonlocal operators and reversible transitions) further illustrate how coupling architecture determines global well-posedness and the bifurcation structure; see [37].

A.2. Demographic stochasticity, diffusion approximations, and the CME framework

Stochastic formulations of population dynamics have a long history, beginning with the birth–death process models of Feller [38] and Bartlett [39], and the systematic development of the CME framework for reaction networks [40, 41].

The diffusion approximation was formalized by Kurtz's limit theorems [19, 20, 42]. This approximation replaces the discrete CTMC with a continuous-path Itô SDE. The drift of this SDE coincides with the deterministic rate equations. Furthermore, the diffusion covariance is determined by the stoichiometry and intensities of the underlying events. This approximation becomes increasingly accurate as the system size parameter Ω grows. The resulting density-level SDE provides the starting point for the LNA and for the stochastic sensitivity analyses developed in this paper. van Kampen's system size expansion [18] and related Ω-expansions [43–45] provide formal perturbative frameworks within which the LNA emerges as the leading-order Gaussian approximation.

For exact stochastic simulation, Gillespie's SSA [46, 47] and its τ-leaping variants [48, 49] generate statistically exact realizations of the CTMC. These serve as the ground truth benchmark against which analytical approximations such as the LNA can be validated.

A.3. *Quasi-cycles and stochastic amplification*

Bartlett [39] and Nisbet and Gurney [50] identified noise-induced quasi-periodic oscillations near a stable focus in an ecological context. This phenomenon, now commonly called a quasi-cycle, was later given a modern spectral characterization through the LNA by McKane and Newman [10] and Boland et al. [11]. The linearized dynamics near a stable spiral point act as a narrow-band filter. These dynamics selectively amplify white demographic noise near the damped oscillation frequency, producing a coherent spectral peak that diverges in height as the Hopf bifurcation is approached.

This amplification mechanism has been studied extensively in both ecological and epidemiological settings. In ecology, quasi-cycles have been analyzed in predator–prey [12, 24, 51] and spatially extended metapopulation frameworks [52–54]. In epidemiology, the closely analogous phenomenon of stochastic resonance in susceptible–infected–recovered (SIR)-type models has been studied by Alonso et al. [55], Rozhnova and Nunes [56], and Black and McKane [57], among others. A unifying perspective on noise amplification near bifurcations in low-dimensional stochastic systems has been provided by several reviews [58–60].

A.4. *Early-warning signals and noisy precursors of bifurcations*

The idea that statistical signatures in stochastic time series can provide advanced warning of approaching tipping points has generated intense interest. This research area has expanded significantly over the past two decades [17, 61, 62]. Generic early warning indicators have been proposed as model-independent precursors of fold and transcritical bifurcations [63–65]. These indicators include increases in autocorrelation, variance, and return time, a phenomenon known as critical slowing down. For Hopf bifurcations specifically, the growing coherence and amplitude of quasi-cycles in the pre-bifurcation regime provide an additional spectral indicator [66, 67].

B. LNA matrix PSD: Fourier domain derivation

This appendix derives the matrix-valued PSD formula used in Section 5 for the LNA near the coexistence equilibrium. We make the Fourier convention explicit and record the symmetry properties.

B.1. *OU form of the LNA and stationarity conditions*

In the LNA, fluctuations $y(t) \in \mathbb{R}^2$ around the coexistence equilibrium satisfy the OU SDE

$$dy(t) = J\,y(t)\,dt + B\,dW(t), \tag{B.1}$$

where $J \in \mathbb{R}^{2\times2}$ is the Jacobian matrix evaluated at the coexistence equilibrium, $B \in \mathbb{R}^{2\times r}$ is any matrix factorization of the local diffusion covariance D_* i.e., $D_* = BB^\top$, and $W(t) \in \mathbb{R}^r$ is a standard r-dimensional Brownian motion.

The PSD formula in the main text is a stationary OU result and therefore applies only when J is Hurwitz (all eigenvalues have strictly negative real parts). In the present paper, this corresponds to the deterministically stable coexistence regime Λ_2 (Section 2). If J is not Hurwitz (e.g., in the post-Hopf regime Λ_1), the stationary covariance and stationary PSD around the coexistence equilibrium are not defined.

B.2. Fourier transform convention and definition of the matrix PSD

We use the Fourier transform convention

$$\widehat{u}(\omega) = \int_{-\infty}^{\infty} e^{-i\omega t} u(t)\, dt, \qquad u(t) = \frac{1}{2\pi} \int_{-\infty}^{\infty} e^{i\omega t} \widehat{u}(\omega)\, d\omega. \tag{B.2}$$

For a weakly stationary vector process $y(t)$, define the covariance function

$$R(\tau) := \mathbb{E}[y(t+\tau)y(t)^{\top}], \tag{B.3}$$

which is independent of t. The matrix-valued PSD is the Fourier transform of $R(\tau)$:

$$S(\omega) = \int_{-\infty}^{\infty} e^{-i\omega\tau} R(\tau)\, d\tau, \qquad R(\tau) = \frac{1}{2\pi} \int_{-\infty}^{\infty} e^{i\omega\tau} S(\omega)\, d\omega. \tag{B.4}$$

Under this convention, no additional 2π factor appears in the forward transform for $S(\omega)$; the 2π factor appears only in the inverse transform.

B.3. Transfer-function derivation of the matrix PSD

We derive the PSD formula via the standard transfer-function representation of the stationary OU process. Formally differentiating (B.1) in the sense of generalized stochastic processes gives

$$\dot{y}(t) = J\,y(t) + B\,\xi(t), \tag{B.5}$$

where $\xi(t) := \dot{W}(t)$ is the r-dimensional Gaussian white noise with the covariance

$$\mathbb{E}[\xi(t)\xi(s)^{\top}] = \delta(t-s) I_r. \tag{B.6}$$

Taking the Fourier transforms of (B.5) yields

$$(i\omega I - J)\widehat{y}(\omega) = B\,\widehat{\xi}(\omega),$$

and hence

$$\widehat{y}(\omega) = H(\omega)\widehat{\xi}(\omega), \qquad H(\omega) := (i\omega I - J)^{-1} B. \tag{B.7}$$

Since the white noise input has the (matrix) spectral density I_r, the output PSD is

$$S(\omega) = H(\omega)\, I_r\, H(\omega)^{\dagger} = [(i\omega I - J)^{-1} B][(i\omega I - J)^{-1} B]^{\dagger}, \tag{B.8}$$

where $(\cdot)^{\dagger}$ denotes the conjugate transpose.

Using $D_* = BB^{\top}$ and the identities

$$(i\omega I - J)^{-1} = -(J - i\omega I)^{-1}, \qquad [(i\omega I - J)^{-1}]^{\dagger} = (-i\omega I - J^{\top})^{-1} = -(J^{\top} + i\omega I)^{-1},$$

the minus signs cancel, yielding the following matrix PSD formula used in the main text:

$$S(\omega) = (J - i\omega I)^{-1} D_* (J^{\top} + i\omega I)^{-1}, \qquad \omega \in \mathbb{R}. \tag{B.9}$$

Because J and D_* are real matrices and $D_* = D_*^{\top}$, the matrix PSD satisfies the Hermitian symmetry

$$S(-\omega) = S(\omega)^{\dagger}. \tag{B.10}$$

Equivalently, the real parts of diagonal entries are even functions of ω, and the imaginary parts of off-diagonal entries are odd (with the corresponding conjugacy relations).

C. Stationary covariance from the 2×2 Lyapunov equation and SSF ellipse formulas

This appendix provides an explicit scheme for the stationary covariance in the 2×2 LNA/OU system, together with the SSF ellipse formulas, and the noisy precursor indicator Π_p used in the main text. The notation is fully aligned with Section 5: J denotes the Jacobian at the coexistence equilibrium, D_* the local diffusion covariance, and W is the stationary covariance of the LNA fluctuations.

C.1. LNA/OU setup and Lyapunov equation

In the deterministically stable coexistence regime (J Hurwitz), the LNA fluctuations $y_t = x_t - K_3$ satisfy the OU SDE

$$dy_t = J\,y_t\,dt + B\,dW_t, \qquad BB^\top = D_*, \tag{C.1}$$

where $J, D_* \in \mathbb{R}^{2\times 2}$, $D_* = D_*^\top$, and W_t is a standard Brownian motion of a suitable dimension.

The stationary covariance matrix

$$W := \mathbb{E}[y_t y_t^\top] = \begin{pmatrix} w_{11} & w_{12} \\ w_{12} & w_{22} \end{pmatrix}$$

is the unique symmetric solution of the continuous Lyapunov equation

$$JW + WJ^\top + D_* = 0. \tag{C.2}$$

Write

$$J = \begin{pmatrix} \alpha & \beta \\ \gamma & \delta \end{pmatrix}, \qquad D_* = \begin{pmatrix} q_{11} & q_{12} \\ q_{12} & q_{22} \end{pmatrix}. \tag{C.3}$$

Expanding (C.2) entrywise and using the symmetry of W gives

$$2\alpha\,w_{11} + 2\beta\,w_{12} = -q_{11}, \tag{C.4a}$$

$$\gamma\,w_{11} + (\alpha + \delta)\,w_{12} + \beta\,w_{22} = -q_{12}, \tag{C.4b}$$

$$2\gamma\,w_{12} + 2\delta\,w_{22} = -q_{22}. \tag{C.4c}$$

Equivalently, we have

$$\underbrace{\begin{pmatrix} 2\alpha & 2\beta & 0 \\ \gamma & \alpha+\delta & \beta \\ 0 & 2\gamma & 2\delta \end{pmatrix}}_{=:\mathcal{M}} \begin{pmatrix} w_{11} \\ w_{12} \\ w_{22} \end{pmatrix} = -\begin{pmatrix} q_{11} \\ q_{12} \\ q_{22} \end{pmatrix}. \tag{C.5}$$

Thus

$$\begin{pmatrix} w_{11} \\ w_{12} \\ w_{22} \end{pmatrix} = -\mathcal{M}^{-1} \begin{pmatrix} q_{11} \\ q_{12} \\ q_{22} \end{pmatrix}, \tag{C.6}$$

whenever $\mathcal{M}$ is invertible.

A direct computation yields

$$\det(\mathcal{M}) = 4(\alpha + \delta)(\alpha\delta - \beta\gamma) = 4\ \mathrm{tr}(J)\ \det(J). \tag{C.7}$$

Hence, if J is Hurwitz (in the 2×2 case, equivalently, $\mathrm{tr}(J) < 0$ and $\det(J) > 0$), then $\det(\mathcal{M}) \neq 0$, and the Lyapunov equation (C.2) has a unique symmetric solution W. This is the regime in which the stationary LNA covariance, PSD, and SSF diagnostics are defined in the main text (Section 5).

C.2. SSF confidence ellipse and principal axis geometry

For a confidence level $p \in (0, 1)$, the SSF confidence ellipse in the deviation coordinates is

$$\mathcal{E}_p = \left\{ z \in \mathbb{R}^2 : \ z^\top W^{-1} z \leq \chi_2^2(p) \right\}, \tag{C.8}$$

where $\chi_2^2(p)$ is the p-quantile of the chi-square distribution with two degrees of freedom.

Let $\lambda_+(W) \geq \lambda_-(W) > 0$ be the eigenvalues of W. For a 2×2 symmetric matrix

$$\lambda_\pm(W) = \frac{w_{11} + w_{22}}{2} \pm \frac{1}{2}\sqrt{(w_{11} - w_{22})^2 + 4w_{12}^2}. \tag{C.9}$$

The corresponding semi-axis lengths are

$$\ell_\pm = \sqrt{\chi_2^2(p)\,\lambda_\pm(W)}. \tag{C.10}$$

A robust expression for the principal axis angle θ (measured from the N-axis to the major axis of the ellipse) is

$$\theta = \frac{1}{2}\,\mathrm{atan2}(2w_{12},\ w_{11} - w_{22}), \tag{C.11}$$

where $\mathrm{atan2}(y, x) \in (-\pi, \pi]$ is the two-argument arctangent. This is preferable to using $\tan(2\theta) = 2w_{12}/(w_{11} - w_{22})$ directly, because atan2 handles the quadrant correctly and is more robust when $w_{11} \approx w_{22}$.

Alternatively, θ may be obtained from the normalized eigenvector associated with $\lambda_+(W)$. The two definitions agree up to the sign/orientation convention $\theta \sim \theta + \pi$.

C.3. noisy precursor indicator Π_p

The noisy precursor indicator used in the main text is

$$\Pi_p = \frac{\ell_+}{d_{\mathrm{sep}}}, \tag{C.12}$$

where ℓ_+ is the length of the major semi-axis from (C.10) and d_{sep} is a problem-dependent distance from the equilibrium to an extinction-relevant or basin-separating boundary (in deviation coordinates).

C.4. Implementation recipe (Lyapunov to SSF to the noisy precursor indicator)

For reproducibility, we summarize the steps used in the paper in Algorithm 1.

Algorithm 1 Computation of W, SSF ellipse, and the noisy precursor indicator in the 2×2 LNA

```
Require: Coexistence equilibrium $K_3$, Jacobian $J = J(K_3)$, local covariance $D_* = a(K_3)$, confidence level $p$
Ensure: Stationary covariance $W$, ellipse semi-axes $\ell_\pm$, angle $\theta$, indicator $\Pi_p$ (if $d_{\mathrm{sep}}$ is specified)
Check Hurwitz condition for $J$ (equivalently in $2 \times 2$: $\mathrm{tr}(J) < 0$ and $\det(J) > 0$)
if Hurwitz fails then
    Return "stationary LNA diagnostics not defined"
end if
Form $\mathcal{M}$ in (C.5) and solve for $(w_{11}, w_{12}, w_{22})^\top$
Construct $W = \begin{pmatrix} w_{11} & w_{12} \\ w_{12} & w_{22} \end{pmatrix}$ and (optionally) symmetrize numerically
Compute the eigenvalues $\lambda_\pm(W)$ from (C.9)
Compute the semi-axis lengths $\ell_\pm$ from (C.10)
Compute the major axis angle $\theta = \frac{1}{2}\,\mathrm{atan2}(2w_{12},\ w_{11} - w_{22})$
if $d_{\mathrm{sep}}$ is specified then
    Compute $\Pi_p = \ell_+ / d_{\mathrm{sep}}$
end if
```

In implementation, it is useful to verify that W is positive definite (within numerical tolerance) and that $\lambda_\pm(W) > 0$ in the Hurwitz regime. Small symmetry violations due to floating-point roundoff can be removed by replacing W with $(W + W^\top)/2$ before spectral decomposition.

D. Implementation-level summary of covariance closures: The full-covariance model versus the diagonal comparator

This appendix summarizes the diffusion coefficients, with emphasis on the precise definition of the full-covariance model and the diagonal noise comparator. The goal is modeling transparency: Both models use the same deterministic drift and differ only in the diffusion covariance structure associated with predation conversion events.

D.1. Common drift and notation

Let $x = (N, P)^\top \in (0, \infty)^2$ denote prey and predator densities, and let $\Omega > 0$ be the system-size parameter. Throughout the paper, both stochastic models (full covariance and diagonal comparator) use the same reduced R–M drift:

$$b(x) = \begin{pmatrix} N\left(1 - \dfrac{N}{k}\right) - \dfrac{mNP}{1+N} \\ P\left(-c + \dfrac{mN}{1+N}\right) \end{pmatrix}. \tag{D.1}$$

Define the predation intensity

$$f_{\mathrm{pred}}(x) := \frac{mNP}{1+N}. \tag{D.2}$$

For compact comparison, we decompose the diffusion covariance into a shared non-predation part and a predation-induced part:

$$a(x) = a_0(x) + a_{\text{pred}}(x). \tag{D.3}$$

When we fix ($e = 1$), the shared non-predation contribution is

$$a_0(x) = \frac{1}{\Omega}\begin{pmatrix} N + \dfrac{N^2}{k} & 0 \\ 0 & cP \end{pmatrix}, \tag{D.4}$$

corresponding to the prey birth, prey competition death, and predator death channels.

D.2. General-e formulas

We first record the covariance formulas with the explicit conversion efficiency $e \in (0, 1]$, which clarifies the relationship between the coupled and split-channel closures.

For the Bernoulli-coupled predation conversion mechanism, in which successful conversion occurs with probability e, the contribution of predation to the density diffusion covariance is

$$a^{(B)}_{\text{pred}}(x) = \frac{1}{\Omega} f_{\text{pred}}(x)\begin{pmatrix} 1 & -e \\ -e & e \end{pmatrix}. \tag{D.5}$$

The effective coupled diffusion-level closure, with the stoichiometric increment $\nu_{\text{eff}} = (-1, e)^\top$, has the following contribution of predation covariance:

$$a^{(\text{eff})}_{\text{pred}}(x) = \frac{1}{\Omega} f_{\text{pred}}(x)\begin{pmatrix} 1 & -e \\ -e & e^2 \end{pmatrix}. \tag{D.6}$$

For the split-channel comparator, consisting of independent prey-removal and predator-birth channels and drift-matched to the same deterministic model, the contribution of predation to covariance is

$$a^{(S)}_{\text{pred}}(x) = \frac{1}{\Omega} f_{\text{pred}}(x)\begin{pmatrix} 1 & 0 \\ 0 & e \end{pmatrix}. \tag{D.7}$$

The coupled closures (D.5) and (D.6) have a strictly negative prey–predator cross-covariance for $N, P > 0$,

$$(a_{\text{pred}})_{12}(x) < 0,$$

whereas the split-channel comparator (D.7) has

$$(a^{(S)}_{\text{pred}})_{12}(x) = 0.$$

This is the key covariance structure difference carried into the Lyapunov/PSD/SSF diagnostics.

D.3. Closures used in this paper and a definition of "fair comparison"

In the main text, we compare a full-covariance diffusion model, which uses a mechanistically coupled predation conversion closure, with a diagonal noise comparator using a drift-matched split-channel closure. This comparison is conducted under identical deterministic drift $b(x)$ (D.1), with the same parameter values (m, c, k, Ω), initial conditions, time discretization, burn-in and sampling windows, and Monte Carlo replication counts. The sole difference between the two models lies in the covariance structure of the diffusion term, specifically the predation-induced off-diagonal covariance and its associated geometry.

E. Explicit Jacobian at the coexistence equilibrium K_3

Because the LNA, Lyapunov covariance, and PSD diagnostics all depend on

$$J = J(K_3),$$

we record here the explicit Jacobian entries for the nondimensional R–M system used throughout the paper and verify the Hopf-threshold sign change of $\mathrm{tr}(J(K_3))$.

E.1. Deterministic drift and general Jacobian

The deterministic R–M system is

$$\begin{cases} \dfrac{dN}{dt} = f(N,P) = N\left(1 - \dfrac{N}{k}\right) - \dfrac{mNP}{1+N}, \\ \dfrac{dP}{dt} = g(N,P) = P\left(-c + \dfrac{mN}{1+N}\right). \end{cases} \tag{E.1}$$

Its Jacobian matrix is

$$J(N,P) = \begin{pmatrix} f_N(N,P) & f_P(N,P) \\ g_N(N,P) & g_P(N,P) \end{pmatrix} = \begin{pmatrix} 1 - \dfrac{2N}{k} - \dfrac{mP}{(1+N)^2} & -\dfrac{mN}{1+N} \\ \dfrac{mP}{(1+N)^2} & -c + \dfrac{mN}{1+N} \end{pmatrix}. \tag{E.2}$$

E.2. Coexistence equilibrium and useful identities

When the coexistence equilibrium exists, it is

$$K_3 = (N^*, P^*) = \left(\frac{c}{m-c}, \frac{k(m-c) - c}{k(m-c)^2}\right), \tag{E.3}$$

under the feasibility conditions $m > c$ and $k(m-c) > c$.

At K_3, the following identities are repeatedly useful:

$$1 + N^* = 1 + \frac{c}{m-c} = \frac{m}{m-c}, \qquad \frac{N^*}{1+N^*} = \frac{c}{m}, \qquad \frac{1}{(1+N^*)^2} = \frac{(m-c)^2}{m^2}. \tag{E.4}$$

Moreover, the predators' isocline condition implies

$$g_P(K_3) = -c + \frac{mN^*}{1+N^*} = 0. \tag{E.5}$$

E.3. Explicit entries of $J(K_3)$

Write

$$J(K_3) = \begin{pmatrix} \alpha & \beta \\ \gamma & \delta \end{pmatrix}. \tag{E.6}$$

Substituting (N^*, P^*) into (E.2) gives:

$$\beta = -\frac{mN^*}{1+N^*} = -c, \tag{E.7}$$

$$\delta = -c + \frac{mN^*}{1+N^*} = 0, \tag{E.8}$$

and

$$\gamma = \frac{mP^*}{(1+N^*)^2} = \frac{m}{(1+N^*)^2} \cdot \frac{k(m-c)-c}{k(m-c)^2} = \frac{k(m-c)-c}{km}. \tag{E.9}$$

For the (1, 1)-entry, one may simplify directly or use $mP^*/(1+N^*)^2 = \gamma$:

$$\begin{aligned} \alpha &= 1 - \frac{2N^*}{k} - \frac{mP^*}{(1+N^*)^2} \\ &= 1 - \frac{2c}{k(m-c)} - \frac{k(m-c)-c}{km} \\ &= \frac{c\,[\,k(m-c)-(m+c)\,]}{km(m-c)}. \end{aligned} \tag{E.10}$$

Hence

$$J(K_3) = \begin{pmatrix} \dfrac{c\,[\,k(m-c)-(m+c)\,]}{km(m-c)} & -c \\ \dfrac{k(m-c)-c}{km} & 0 \end{pmatrix}. \tag{E.11}$$

E.4. Trace, determinant, and Hopf threshold sign change

From (E.11), we have

$$\operatorname{tr}(J(K_3)) = \alpha = \frac{c\,[\,k(m-c)-(m+c)\,]}{km(m-c)}. \tag{E.12}$$

Therefore, defining

$$k_H = \frac{m+c}{m-c}, \tag{E.13}$$

we obtain the factorized form

$$\operatorname{tr}(J(K_3)) = \frac{c}{km(m-c)}\,(m-c)\,(k-k_H) = \frac{c}{km}\,(k-k_H). \tag{E.14}$$

Since $c > 0$, $k > 0$, and $m > 0$, this makes the sign change explicit as follows

$$\operatorname{tr}(J(K_3)) < 0 \iff k < k_H, \qquad \operatorname{tr}(J(K_3)) = 0 \iff k = k_H, \qquad \operatorname{tr}(J(K_3)) > 0 \iff k > k_H. \tag{E.15}$$

The determinant is

$$\det(J(K_3)) = \alpha\delta - \beta\delta = c\,\gamma = \frac{c\,[\,k(m-c)-c\,]}{km}, \tag{E.16}$$

which is strictly positive under the coexistence feasibility condition $k(m-c) > c$. Thus, in the coexistence regime, local stability is governed by the sign of the trace, and the enrichment-driven Hopf threshold occurs at $k = k_H$, as used throughout the main text.

F. Technical proofs for the covariance structure results in Section 3

This appendix provides detailed calculations and proofs for the structural covariance results stated in Section 3, with particular emphasis on the mechanistic origin of the negative prey–predator cross-covariance under coupled predation conversion closures. The purpose is to make the key claims in the main text fully verifiable and citable.

Throughout, we write

$$x = (N, P) \in D = (0, \infty)^2, \qquad f_{\mathrm{pred}}(x) := \frac{mNP}{1+N},$$

and recall the density-level covariance identity

$$a(x) = \frac{1}{\Omega} \sum_{k=1}^{K} f_k(x)\, \nu_k \nu_k^{\top} = \frac{1}{\Omega} S \,\mathrm{diag}(f(x))\, S^{\top}. \tag{F.1}$$

In this appendix, $a_{\mathrm{pred}}(\cdot)$ denotes the contribution to $a(\cdot)$ coming only from predation-related channels.

F.1. Predation covariance under the Bernoulli-coupled closure

Recall the Bernoulli-coupled exact CTMC predation channels used in Section 3:

$$\nu_4^{(B)} = \begin{pmatrix} -1 \\ 1 \end{pmatrix}, \qquad \nu_5^{(B)} = \begin{pmatrix} -1 \\ 0 \end{pmatrix},$$

with the density-level intensities

$$f_4^{(B)}(x) = e\, f_{\mathrm{pred}}(x), \qquad f_5^{(B)}(x) = (1-e)\, f_{\mathrm{pred}}(x), \qquad e \in (0, 1].$$

Therefore, the contribution of predation to the diffusion covariance is

$$a_{\mathrm{pred}}^{(B)}(x) = \frac{1}{\Omega} \left[f_4^{(B)}(x)\, \nu_4^{(B)} (\nu_4^{(B)})^{\top} + f_5^{(B)}(x)\, \nu_5^{(B)} (\nu_5^{(B)})^{\top} \right]. \tag{F.2}$$

We compute the rank-one matrices explicitly as follows

$$\nu_4^{(B)} (\nu_4^{(B)})^{\top} = \begin{pmatrix} -1 \\ 1 \end{pmatrix} \begin{pmatrix} -1 & 1 \end{pmatrix} = \begin{pmatrix} 1 & -1 \\ -1 & 1 \end{pmatrix}, \tag{F.3}$$

$$\nu_5^{(B)} (\nu_5^{(B)})^{\top} = \begin{pmatrix} -1 \\ 0 \end{pmatrix} \begin{pmatrix} -1 & 0 \end{pmatrix} = \begin{pmatrix} 1 & 0 \\ 0 & 0 \end{pmatrix}. \tag{F.4}$$

Substituting (F.3) and (F.4) into (F.2) gives

$$\begin{aligned} a_{\mathrm{pred}}^{(B)}(x) &= \frac{1}{\Omega} \left[e f_{\mathrm{pred}}(x) \begin{pmatrix} 1 & -1 \\ -1 & 1 \end{pmatrix} + (1-e) f_{\mathrm{pred}}(x) \begin{pmatrix} 1 & 0 \\ 0 & 0 \end{pmatrix} \right] \\ &= \frac{f_{\mathrm{pred}}(x)}{\Omega} \left[\begin{pmatrix} e & -e \\ -e & e \end{pmatrix} + \begin{pmatrix} 1-e & 0 \\ 0 & 0 \end{pmatrix} \right] \end{aligned}$$

$$= \frac{f_{\text{pred}}(x)}{\Omega} \begin{pmatrix} 1 & -e \\ -e & e \end{pmatrix}. \tag{F.5}$$

Equivalently, we have

$$a^{(B)}_{\text{pred}}(x) = \frac{1}{\Omega} \frac{mNP}{1+N} \begin{pmatrix} 1 & -e \\ -e & e \end{pmatrix}. \tag{F.6}$$

Hence, the off-diagonal entry is

$$(a^{(B)}_{\text{pred}}(x))_{12} = -\frac{1}{\Omega}\, e\, \frac{mNP}{1+N}. \tag{F.7}$$

In particular, for $x \in D$ and $e \in (0, 1]$, we have

$$(a^{(B)}_{\text{pred}}(x))_{12} < 0. \tag{F.8}$$

F.2. Predation covariance under the effective coupled $(-1, e)^\top$ *closure*

For the effective diffusion-level coupled closure, the predation channel is represented by

$$\nu_{\text{eff}} = \begin{pmatrix} -1 \\ e \end{pmatrix}, \qquad f_{\text{eff}}(x) = f_{\text{pred}}(x) = \frac{mNP}{1+N}.$$

Its contribution of predation to covariance is

$$a^{(\text{eff})}_{\text{pred}}(x) = \frac{1}{\Omega} f_{\text{pred}}(x)\, \nu_{\text{eff}} \nu_{\text{eff}}^\top. \tag{F.9}$$

Computing the outer product, we have

$$\nu_{\text{eff}} \nu_{\text{eff}}^\top = \begin{pmatrix} -1 \\ e \end{pmatrix} \begin{pmatrix} -1 & e \end{pmatrix} = \begin{pmatrix} 1 & -e \\ -e & e^2 \end{pmatrix}. \tag{F.10}$$

Substituting (F.10) into (F.9), we obtain

$$a^{(\text{eff})}_{\text{pred}}(x) = \frac{1}{\Omega} \frac{mNP}{1+N} \begin{pmatrix} 1 & -e \\ -e & e^2 \end{pmatrix}. \tag{F.11}$$

Therefore, the off-diagonal entry is

$$(a^{(\text{eff})}_{\text{pred}}(x))_{12} = -\frac{1}{\Omega}\, e\, \frac{mNP}{1+N}, \tag{F.12}$$

which is strictly negative on D for $e \in (0, 1]$.

F.3. Predation covariance under the split-channel comparator

For the split-channel comparator, predation-related prey removal and predator birth are modeled as independent channels as follows

$$\nu^{(S)}_4 = \begin{pmatrix} -1 \\ 0 \end{pmatrix}, \qquad \nu^{(S)}_5 = \begin{pmatrix} 0 \\ 1 \end{pmatrix},$$

with the intensities

$$f_4^{(S)}(x) = f_{\mathrm{pred}}(x), \qquad f_5^{(S)}(x) = e\, f_{\mathrm{pred}}(x).$$

The predation covariance contribution is

$$a_{\mathrm{pred}}^{(S)}(x) = \frac{1}{\Omega}\left[f_4^{(S)}(x)\, v_4^{(S)}(v_4^{(S)})^\top + f_5^{(S)}(x)\, v_5^{(S)}(v_5^{(S)})^\top\right]. \tag{F.13}$$

Now

$$v_4^{(S)}(v_4^{(S)})^\top = \begin{pmatrix}-1\\0\end{pmatrix}\begin{pmatrix}-1 & 0\end{pmatrix} = \begin{pmatrix}1 & 0\\0 & 0\end{pmatrix}, \tag{F.14}$$

$$v_5^{(S)}(v_5^{(S)})^\top = \begin{pmatrix}0\\1\end{pmatrix}\begin{pmatrix}0 & 1\end{pmatrix} = \begin{pmatrix}0 & 0\\0 & 1\end{pmatrix}. \tag{F.15}$$

Hence

$$\begin{aligned} a_{\mathrm{pred}}^{(S)}(x) &= \frac{1}{\Omega}\left[f_{\mathrm{pred}}(x)\begin{pmatrix}1 & 0\\0 & 0\end{pmatrix} + e f_{\mathrm{pred}}(x)\begin{pmatrix}0 & 0\\0 & 1\end{pmatrix}\right] \\ &= \frac{1}{\Omega}\,\frac{mNP}{1+N}\begin{pmatrix}1 & 0\\0 & e\end{pmatrix}. \end{aligned} \tag{F.16}$$

Therefore,

$$(a_{\mathrm{pred}}^{(S)}(x))_{12} = 0. \tag{F.17}$$

This confirms that the split-channel model is drift-compatible with the coupled closures (after parameter matching) but removes the same-event prey–predator covariance at the predation level.

F.4. A general proposition: Drift equivalence does not imply covariance equivalence

We now record an abstract statement (valid in an arbitrary dimension) that formalizes the distinction used repeatedly in Section 3.

Proposition F.1 (Drift equivalence does not imply covariance equivalence)**.** *Fix $d \in \mathbb{N}$, $\Omega > 0$, and let x be a state parameter. Consider the two-channel representations*

$$\{(v_k, f_k(x))\}_{k=1}^{K} \quad \textit{and} \quad \{(\tilde v_\ell, \tilde f_\ell(x))\}_{\ell=1}^{\tilde K},$$

with $v_k, \tilde v_\ell \in \mathbb{R}^d$, and non-negative intensities $f_k(x), \tilde f_\ell(x) \geq 0$. Define their diffusion drifts and covariances by

$$b(x) := \sum_{k=1}^{K} f_k(x)\, v_k, \qquad a(x) := \frac{1}{\Omega}\sum_{k=1}^{K} f_k(x)\, v_k v_k^\top, \tag{F.18}$$

$$\tilde b(x) := \sum_{\ell=1}^{\tilde K} \tilde f_\ell(x)\, \tilde v_\ell, \qquad \tilde a(x) := \frac{1}{\Omega}\sum_{\ell=1}^{\tilde K} \tilde f_\ell(x)\, \tilde v_\ell \tilde v_\ell^\top. \tag{F.19}$$

Then $b(x) = \tilde b(x)$ does not, in general, imply $a(x) = \tilde a(x)$.

More precisely, the equality of drifts imposes equality of the first moments of the channel increments, while the equality of covariances additionally requires the equality of the corresponding second-moment tensors as follows

$$\sum_{k=1}^{K} f_k(x)\, \nu_k = \sum_{\ell=1}^{\tilde{K}} \tilde{f}_\ell(x)\, \tilde{\nu}_\ell \quad \not\Longrightarrow \quad \sum_{k=1}^{K} f_k(x)\, \nu_k \nu_k^\top = \sum_{\ell=1}^{\tilde{K}} \tilde{f}_\ell(x)\, \tilde{\nu}_\ell \tilde{\nu}_\ell^\top .$$

Proof. The claim is immediate from the definitions (F.18)–(F.19): Drift depends on weighted first moments of channel increments, whereas the covariance depends on weighted second moments.

To show strict non-implication, it suffices to provide a counterexample. In dimension $d = 2$, fix a scalar $r > 0$ and compare:

$$\text{Representation I:} \quad (\nu, f) = \left(\begin{pmatrix} -1 \\ 1 \end{pmatrix}, r \right),$$

with

$$\text{Representation II:} \quad (\tilde{\nu}_1, \tilde{f}_1) = \left(\begin{pmatrix} -1 \\ 0 \end{pmatrix}, r \right), \qquad (\tilde{\nu}_2, \tilde{f}_2) = \left(\begin{pmatrix} 0 \\ 1 \end{pmatrix}, r \right).$$

Then both representations produce the same drift,

$$b = \tilde{b} = r \begin{pmatrix} -1 \\ 1 \end{pmatrix},$$

but their covariance matrices differ:

$$a = \frac{r}{\Omega} \begin{pmatrix} 1 & -1 \\ -1 & 1 \end{pmatrix}, \qquad \tilde{a} = \frac{r}{\Omega} \begin{pmatrix} 1 & 0 \\ 0 & 1 \end{pmatrix}.$$

In particular, $a_{12} = -r/\Omega \neq 0 = \tilde{a}_{12}$, so $a \neq \tilde{a}$. □

Remark F.1 (Relevance to the predation closures in this paper)**.** *Proposition F.1 is precisely the mechanism behind the distinction between the coupled predation closures (Bernoulli-coupled exact CTMC and effective* $(-1, e)^\top$ *diffusion closure) and the split-channel comparator. These constructions are drift-compatible after parameter matching, but their predation-related covariance contributions differ because their channel increment second moments differ.*

F.5. Structural sign proposition for the predation-induced cross-covariance

We now state and prove the structural sign result underlying the main text discussion.

Proposition F.2 (Structural negativity of the predation-induced prey–predator cross-covariance)**.** *Let* $x = (N, P) \in D = (0, \infty)^2$, $\Omega > 0$, $m > 0$, *and* $e \in (0, 1]$. *For the predation-related contribution to covariance we have the following.*

(i) Under the Bernoulli-coupled closure, we have

$$(a^{(B)}_{\text{pred}}(x))_{12} = -\frac{1}{\Omega}\, e\, \frac{mNP}{1+N} < 0.$$

(ii) Under the effective coupled $(-1, e)$ *closure, we have*

$$(a_{\text{pred}}^{(\text{eff})}(x))_{12} = -\frac{1}{\Omega}\, e\, \frac{mNP}{1+N} < 0.$$

(iii) Under the split-channel comparator, we have

$$(a_{\text{pred}}^{(S)}(x))_{12} = 0.$$

Consequently, the negative predation-induced prey–predator cross-covariance is a structural signature of same-event prey-loss/predator-gain coupling, and is absent in the split-channel representation that decouples those increments.

Proof. Parts (i)–(iii) are immediate from the explicit formulas (F.6), (F.11), and (F.16), respectively. Since $x \in D$ implies $N > 0$ and $P > 0$, and since $m > 0$, $e \in (0, 1]$, and $\Omega > 0$, the quantity

$$\frac{1}{\Omega}\, e\, \frac{mNP}{1+N}$$

is strictly positive; therefore, the off-diagonal terms in (i) and (ii) are strictly negative. □

Corollary F.1 (Cross-covariance agreement of Bernoulli-coupled and effective coupled closures)**.** *Under the assumptions of Proposition F.2, we have*

$$(a_{\text{pred}}^{(B)}(x))_{12} = (a_{\text{pred}}^{(\text{eff})}(x))_{12} = -\frac{1}{\Omega}\, e\, \frac{mNP}{1+N}.$$

Thus, the effective $(-1, e)^{\top}$ *closure preserves the predation-induced cross-covariance exactly, even though it is not an exact integer-valued CTMC jump representation when* $e \notin \mathbb{N}$*.*

Proof. Compare the off-diagonal entries in (F.6) and (F.11). □

Remark F.2 (Predator-variance difference between Bernoulli-coupled and effective coupled closures)**.** *Although Corollary F.1 shows the exact agreement of the predation-induced cross-covariance, the predator variance entries differ:*

$$(a_{\text{pred}}^{(B)}(x))_{22} = \frac{1}{\Omega}\, e\, f_{\text{pred}}(x), \qquad (a_{\text{pred}}^{(\text{eff})}(x))_{22} = \frac{1}{\Omega}\, e^2\, f_{\text{pred}}(x).$$

This is the variance-level distinction noted in the main text: The effective $(-1, e)^{\top}$ *closure preserves the coupled fluctuation direction and cross-term but not the exact Bernoulli offspring variance.*

F.6. Matrix-level decomposition viewpoint

For later reference, it is sometimes convenient to decompose the full covariance into the contributions of nonpredation and predation as follows:

$$a(x) = a_{\text{base}}(x) + a_{\text{pred}}(x),$$

where $a_{\text{base}}(x)$ collects prey birth, prey competition death, and predator death channels and $a_{\text{pred}}(x)$ is one of

$$a_{\text{pred}}^{(B)}(x), \qquad a_{\text{pred}}^{(\text{eff})}(x), \qquad a_{\text{pred}}^{(S)}(x).$$

Since the base channels in the present construction contribute only diagonal terms, the sign and magnitude of the full off-diagonal covariance $a_{12}(x)$ are determined entirely by the predation component. Therefore, Proposition F.2 directly controls the sign of the full prey–predator cross-covariance in the coupled closures.

References

1. M. L. Rosenzweig, R. H. MacArthur, Graphical representation and stability conditions of predator–prey interactions, *Am. Nat.*, **97** (1963), 209–223. https://doi.org/10.1086/282272
2. R. MacArthur, Species packing and competitive equilibrium for many species, *Theor. Popul. Biol.*, **1** (1970), 1–11. https://doi.org/10.1016/0040-5809(70)90039-0
3. M. L. Rosenzweig, Paradox of enrichment: Destabilization of exploitation ecosystems in ecological time, *Science*, **171** (1971), 385–387. https://doi.org/10.1126/science.171.3969.385
4. M. E. Gilpin, Enriched predator–prey systems: Theoretical stability, *Science*, **177** (1972), 902–904. https://doi.org/10.1126/science.177.4052.902
5. R. M. May, Limit cycles in predator–prey communities, *Science*, **177** (1972), 900–902. https://doi.org/10.1126/science.177.4052.900
6. J. F. Riebesell, Paradox of enrichment in competitive systems, *Ecology*, **55** (1974), 183–187. https://doi.org/10.2307/1934634
7. P. A. Abrams, C. J. Walters, Invulnerable prey and the paradox of enrichment, *Ecology*, **77** (1996), 1125–1133. https://doi.org/10.2307/2265581
8. K. L. Kirk, Enrichment can stabilize population dynamics: Autotoxins and density dependence, *Ecology*, **79** (1998), 2456–2462. https://doi.org/10.1890/0012-9658(1998)079[2456:ECSPDA]2.0.CO;2
9. S. Roy, J. Chattopadhyay, The stability of ecosystems: A brief overview of the paradox of enrichment, *J. Biosci.*, **32** (2007), 421–428. https://doi.org/10.1007/s12038-007-0040-1
10. A. J. McKane, T. J. Newman, Predator–prey cycles from resonant amplification of demographic stochasticity, *Phys. Rev. Lett.*, **94** (2005), 218102. https://doi.org/10.1103/PhysRevLett.94.218102
11. R. P. Boland, T. Galla, A. J. McKane, How limit cycles and quasi-cycles are related in systems with intrinsic noise, *J. Stat. Mech. Theory Exp.*, **2008** (2008), P09001. https://doi.org/10.1088/1742-5468/2008/09/P09001
12. M. Pineda-Krch, H. J. Blok, U. Dieckmann, M. Doebeli, A tale of two cycles-distinguishing quasi-cycles and limit cycles in finite predator–prey populations, *Oikos*, **116** (2007), 53–64. https://doi.org/10.1111/j.2006.0030-1299.14940.x
13. C. Kuehn, A mathematical framework for critical transitions: Bifurcations, fast-slow systems and stochastic dynamics, *Phys. D: Nonlinear Phenom.*, **240** (2011), 1020–1035. https://doi.org/10.1016/j.physd.2011.02.012
14. V. Dakos, S. R. Carpenter, W. A. Brock, A. M. Ellison, V. Guttal, A. R. Ives, et al., Methods for detecting early warnings of critical transitions in time series illustrated using simulated ecological data, *PLoS ONE*, **7** (2012), e41010. https://doi.org/10.1371/journal.pone.0041010

15. C. Boettiger, A. Hastings, Quantifying limits to detection of early warning for critical transitions, *J. R. Soc. Interface*, **9** (2012), 2527–2539. https://doi.org/10.1098/rsif.2012.0125
16. C. Boettiger, A. Hastings, From patterns to predictions, *Nature*, **493** (2013), 157–158. https://doi.org/10.1038/493157a
17. T. M. Lenton, H. Held, E. Kriegler, J. W. Hall, W. Lucht, S. Rahmstorf, et al., Tipping elements in the Earth's climate system, *Proc. Natl. Acad. Sci.*, **105** (2008), 1786–1793. https://doi.org/10.1073/pnas.0705414105
18. N. G. van Kampen, *Stochastic Processes in Physics and Chemistry*, 3^{rd} edition, Elsevier, 2007. https://doi.org/10.1016/B978-0-444-52965-7.X5000-4
19. T. G. Kurtz, Solutions of ordinary differential equations as limits of pure jump markov processes, *J. Appl. Probab.*, **7** (1970), 49–58. https://doi.org/10.2307/3212147
20. T. G. Kurtz, Limit theorems for sequences of jump Markov processes approximating ordinary differential processes, *J. Appl. Probab.*, **8** (1971), 344–356. https://doi.org/10.2307/3211904
21. C. Gardiner, *Stochastic Methods: A Handbook for the Natural and Social Sciences*, 4^{th} edition, Springer, 2009.
22. H. Risken, *The Fokker-Planck Equation: Methods of Solution and Applications*, 2^{nd} edition, Springer, 1996. https://doi.org/10.1007/978-3-642-61544-3
23. C. A. Lugo, A. J. McKane, Quasicycles in a spatial predator–prey model, *Phys. Rev. E*, **78** (2008), 051911. https://doi.org/10.1103/PhysRevE.78.051911
24. A. J. Black, A. J. McKane, Stochastic formulation of ecological models and their applications, *Trends Ecol. Evol.*, **27** (2012), 337–345. https://doi.org/10.1016/j.tree.2012.01.014
25. D. T. Gillespie, The chemical Langevin equation, *J. Chem. Phys.*, **113** (2000), 297–306. https://doi.org/10.1063/1.481811
26. S. N. Ethier, T. G. Kurtz, *Markov Processes: Characterization and Convergence*, Wiley, 1986. https://doi.org/10.1002/9780470316658
27. D. F. Anderson, T. G. Kurtz, *Stochastic Analysis of Biochemical Systems*, 1^{st} edition, Springer, 2015. https://doi.org/10.1007/978-3-319-16895-1
28. L. S. Wang, J. Yu, Analysis framework for stochastic predator–prey model with demographic noise, *Results Appl. Math.*, **27** (2025), 100621. https://doi.org/10.1016/j.rinam.2025.100621
29. A. Chatterjee, M. A. Abbasi, E. Venturino, J. Zhen, M. Haque, A predator–prey model with prey refuge: under a stochastic and deterministic environment, *Nonlinear Dyn.*, **112** (2024), 13667–13693. https://doi.org/10.1007/s11071-024-09756-9
30. S. Pal, M. Banerjee, R. Melnik, Nonequilibrium dynamics in a noise-induced predator–prey model, *Chaos Solitons Fractals*, **191** (2025), 115884. https://doi.org/10.1016/j.chaos.2024.115884
31. W. Li, L. Zhang, J. Cao, F. Xu, Z. Cai, Finite time attractivity and exponentially stable of a multi-stage epidemic system with discontinuous incidence, *Qual. Theory Dyn. Syst.*, **24** (2025), 199. https://doi.org/10.1007/s12346-025-01358-z

32. C. Hauzy, G. Nadin, E. Canard, I. Gounand, N. Mouquet, B. Ebenman, Confronting the paradox of enrichment to the metacommunity perspective, *PLoS ONE*, **8** (2013), e82969. https://doi.org/10.1371/journal.pone.0082969
33. V. A. A. Jansen, Regulation of predator–prey systems through spatial interactions: A possible solution to the paradox of enrichment, *Oikos*, **74** (1995), 384–390. https://doi.org/10.2307/3545983
34. Y. A. Kuznetsov, *Elements of Applied Bifurcation Theory*, 4^{th} edition, 2023. https://doi.org/10.1007/978-3-031-22007-4
35. X. Lin, Y. Xu, D. Gao, G. Fan, Bifurcation and overexploitation in Rosenzweig-MacArthur model, *Discret. Contin. Dyn. Syst. Ser. B*, **28** (2023), 690–706. https://doi.org/10.3934/dcdsb.2022094
36. A. D. Bazykin, *Nonlinear Dynamics of Interacting Populations*, World Scientific, 1998. https://doi.org/10.1142/2284
37. J. Yu, L. S. Wang, Z. Liu, J. Liu, Pattern suppression and recovery under one-way versus two-way chemotactic coupling in hybrid partial differential equation–ordinary differential equation models, *Transp. Phenom.*, (2026),1–26. https://doi.org/10.1515/tp-2026-0023
38. W. Feller, Die grundlagen der volterraschen theorie des kampfes ums dasein in wahrscheinlichkeitstheoretischer behandlung, *Acta Biotheor.*, **5** (1939), 11–40. https://doi.org/10.1007/BF01602932
39. M. S. Bartlett, *Stochastic Population Models in Ecology and Epidemiology*, Wiley, 1960.
40. D. A. McQuarrie, Stochastic approach to chemical kinetics, *J. Appl. Probab.*, **4** (1967), 413–478. https://doi.org/10.2307/3212214
41. D. T. Gillespie, *Markov Processes: An Introduction for Physical Scientists*, Academic Press, 1991. https://doi.org/10.1016/C2009-0-22215-X
42. T. G. Kurtz, Strong approximation theorems for density dependent Markov chains, *Stochastic Process. Appl.*, **6** (1978), 223–240. https://doi.org/10.1016/0304-4149(78)90020-0
43. R. Grima, An effective rate equation approach to reaction kinetics in small volumes: Theory and application to biochemical reactions in nonequilibrium steady-state conditions, *J. Chem. Phys.*, **133** (2010), 035101. https://doi.org/10.1063/1.3454685
44. R. Grima, Construction and accuracy of partial differential equation approximations to the chemical master equation, *Phys. Rev. E*, **84** (2011), 056109. https://doi.org/10.1103/PhysRevE.84.056109
45. P. Thomas, R. Grima, A. V. Straube, Rigorous elimination of fast stochastic variables from the linear noise approximation using projection operators, *Phy. Rev. E*, **86** (2012), 041110. https://doi.org/10.1103/PhysRevE.86.041110
46. D. T. Gillespie, Exact stochastic simulation of coupled chemical reactions, *J. Phys. Chem.*, **81** (1977), 2340–2361. https://doi.org/10.1021/j100540a008
47. D. T. Gillespie, A general method for numerically simulating the stochastic time evolution of coupled chemical reactions, *J. Comput. Phys.*, **22** (1976), 403–434. https://doi.org/10.1016/0021-9991(76)90041-3

48. D. T. Gillespie, Approximate accelerated stochastic simulation of chemically reacting systems, *J. Chem. Phys.*, **115** (2001), 1716–1733. https://doi.org/10.1063/1.1378322
49. Y. Cao, D. T. Gillespie, L. R. Petzold, Efficient step size selection for the tau-leaping simulation method, *J. Chem. Phys.*, **124** (2006), 044109. https://doi.org/10.1063/1.2159468
50. R. M. Nisbet, W. S. C. Gurney, *Modelling Fluctuating Populations*, Wiley, 1982.
51. F. Barraquand, S. Louca, K. C. Abbott, C. A. Cobbold, F. Cordoleani, D. L. DeAngelis, et al., Moving forward in circles: Challenges and opportunities in modelling population cycles, *Ecol. Lett.*, **20** (2017), 1074–1092. https://doi.org/10.1111/ele.12789
52. T. Butler, N. Goldenfeld, Robust ecological pattern formation induced by demographic noise, *Phys. Rev. E*, **80** (2009), 030902. https://doi.org/10.1103/PhysRevE.80.030902
53. T. Biancalani, D. Fanelli, F. Di Patti, Stochastic Turing patterns in the Brusselator model, *Phys. Rev. E*, **81** (2010), 046215. https://doi.org/10.1103/PhysRevE.81.046215
54. T. Biancalani, T. Galla, A. J. McKane, Stochastic waves in a Brusselator model with nonlocal interaction, *Phys. Rev. E*, **84** (2011), 026201. https://doi.org/10.1103/PhysRevE.84.026201
55. D. Alonso, A. J. McKane, M. Pascual, Stochastic amplification in epidemics, *J. R. Soc. Interface*, **4** (2007), 575–582. https://doi.org/10.1098/rsif.2006.0192
56. G. Rozhnova, A. Nunes, Stochastic effects in a seasonally forced epidemic model, *Phys. Rev. E*, **82** (2010), 041906. https://doi.org/10.1103/PhysRevE.82.041906
57. A. J. Black, A. J. McKane, Stochastic amplification in an epidemic model with seasonal forcing, *J. Theor. Biol.*, **267** (2010), 85–94. https://doi.org/10.1016/j.jtbi.2010.08.014
58. A. J. McKane, T. Biancalani, T. Rogers, Stochastic pattern formation and spontaneous polarisation: the linear noise approximation and beyond, *Bull. Math. Biol.*, **76** (2014), 895–921. https://doi.org/10.1007/s11538-013-9827-4
59. R. P. Boland, T. Galla, A. J. McKane, Limit cycles, complex Floquet multipliers, and intrinsic noise, *Phys. Rev. E*, **79** (2009), 051131. https://doi.org/10.1103/PhysRevE.79.051131
60. L. J. S. Allen, *An Introduction to Stochastic Processes with Applications to Biology*, 2^{nd} edition, Chapman and Hall/CRC, 2010. https://doi.org/10.1201/b12537
61. M. Scheffer, J. Bascompte, W. A. Brock, V. Brovkin, S. R. Carpenter, V. Dakos, et al., Early-warning signals for critical transitions, *Nature*, **461** (2009), 53–59. https://doi.org/10.1038/nature08227
62. M. Scheffer, S. R. Carpenter, T. M. Lenton, J. Bascompte, W. Brock, V. Dakos, et al., Anticipating critical transitions, *Science*, **338** (2012), 344–348. https://doi.org/10.1126/science.1225244
63. V. Dakos, M. Scheffer, E. H. Van Nes, V. Brovkin, V. Petoukhov, H. Held, Slowing down as an early warning signal for abrupt climate change, *Proc. Natl. Acad. Sci.*, **105** (2008), 14308–14312. https://doi.org/10.1073/pnas.0802430105
64. H. Held, T. Kleinen, Detection of climate system bifurcations by degenerate fingerprinting, *Geophys. Res. Lett.*, **31** (2004), L23207. https://doi.org/10.1029/2004GL020972
65. C. Wissel, A universal law of the characteristic return time near thresholds, *Oecologia*, **65** (1984), 101–107. https://doi.org/10.1007/BF00384470

66. S. J. Lade, T. Gross, Early warning signals for critical transitions: a generalized modeling approach, *PLoS Comput. Biol.*, **8** (2012), e1002360. https://doi.org/10.1371/journal.pcbi.1002360

67. P. S. Dutta, Y. Sharma, K. C. Abbott, Robustness of early warning signals for catastrophic and non-catastrophic transitions, *Oikos*, **127** (2018), 1251–1263. https://doi.org/10.1111/oik.05172

AIMS Press